Experimental and numerical comparison of water transport in untreated and treated diffusion layers of proton exchange membrane (PEM) fuel cells

CrossMark

Mehdi Shahraeeni, Mina Hoorfar*

University of British Columbia, School of Engineering, Kelowna V1V 1V7, BC, Canada

HIGHLIGHTS

► Fluorescence microscopy is used for ex-situ visualization of flow in GDLs.
► A pore-network model is developed to study saturation in treated and untreated GDLs.
► Three different flow characteristics are identified for treated and untreated GDLs.
► Water rapidly invades the exposed areas and develops new passages in untreated GDLs.
► Water prefers to flow through a limited number of initial passages in treated GDLs.

GRAPHICAL ABSTRACT
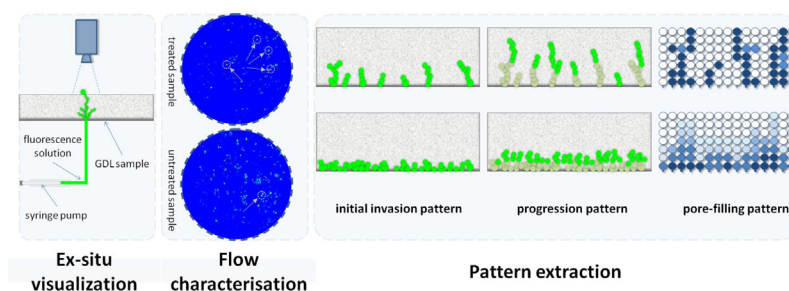
ARTICLE INFO

ABSTRACT

In this paper, a fluorescein solution is injected into the gas diffusion layer (GDL) of a PEM fuel cell to simulate water flow through the porous medium under flooding conditions. The effect of the GDL hydrophobic treatment is studied by analyzing the images obtained from fluorescence microscopy. The intensity of images is correlated to the liquid water content in the medium. As a result, three distinguishable patterns are recognized between the treated and untreated GDL samples. These patterns include: (1) initial invasion, (2) progression and (3) pore filling. Based on the flow characteristics, a pore-network model is developed and applied to unique network geometry with different hydrophobic fractions to study the effect of hydrophobicity on the flow configuration. It is shown that the model predicts the flow configurations which are qualitatively in agreement with the experimental observation. The model is then used to obtain saturation for samples with different hydrophobic fractions. The trend is in agreement with the results reported in the past.

© 2013 Elsevier B.V. All rights reserved.

1. Introduction

Excess water accumulated at the interface of the gas diffusion layer (GDL) and the cathode catalyst layer at high current density covers the active area, limiting the performance of the fuel cell [1–5]. Liquid water penetrates through the GDL toward the flow channels and breaks through at the GDL–flow channel interface. The saturation and capillary pressure associated with water breakthrough determine the resistance of the porous medium to gaseous reactant transport. Liquid water flow in different components of the cell has been studied extensively using both experimental and numerical techniques.

* Corresponding author. Tel.: +1 250 807 8804; fax: +1 250 807 9850.
 E-mail address: mina.hoorfar@ubc.ca (M. Hoorfar).

1.1. Experimental techniques

Different techniques including magnetic resonance imaging (MRI), neutron imaging, X-ray microtomography, direct optical visualization, and fluorescence microscopy have been employed to study water formation and distribution in different components of the cell which may have not been limited to the GDL. For instance, the MRI technique, which is a non-destructive method widely used in medical applications, uses a radio-frequency signal to excite particular nuclei in the presence of a strong static magnetic field. The excited nuclei absorb the signal and resonate accordingly. The measurement of emitted resonance determines the existence of nuclei at a particular location. The MRI technique has been used for liquid water detection and determination of diffusion coefficient in the membrane [6], as well as the measurement of the distribution of water content in the membrane during the operation of the fuel cell [7]. The measurements have shown that the water concentration gradient in the membrane and the overall water content decrease as the cell current increases. Also, the measurement from MRI indicated that the rapid drop in the cell voltage, which occurs within the first 3 min of the experiment, is associated with a decrease in the water content in the anode side of the membrane [6–8]. Effects of the membrane thickness and cell working current on the level of hydration and distribution of water in the membrane have also been studied using the MRI technique [9]. It was shown that a thick membrane is better hydrated than a thin one and the total water content in the membrane decreases for higher current densities [9]. The MRI technique has also been used to study the effect of diffusion in water transport between the catalyst and membrane [10]. The results reveal that radial gradient diffusion removes water from the catalysts into the surrounding membrane. Another use of MRI has been in the study of the effect of the gas flow field configuration on the distribution of water in the membrane and cathode flow field [11]. The results have shown a more uniform distribution of water throughout the electrolyte due to counter-flow configuration. In essence, the maximum power output was obtained when liquid water is first visible in the MRI image of the cathode flow field, and subsequently the power decreases as the liquid water continues to accumulate [11].

The neutron imaging technique is another method which has been used to visualize water inside the network of the fuel cell. In this technique, the material under study is bombarded with beams of neutrons. If water existed in the material the intensity of the neutron beam is impaired. This impairment is proportional to the water content in the material. The technique can be employed while the fuel cell is working in real conditions, and unlike the MRI technique, the neutron imaging is not sensitive to the material used in the fuel cell. However, the cost of this method has limited the use of this technique compared to other visualization techniques [12]. Neutron imaging has been used to study different effects including water distribution along the thickness of the membrane [13]; production, transport and removal of water throughout the cell components [14]; and visualization of two-phase flow in an operating PEM fuel cell [15]. Using neutron imaging, Pekula et al. [15] have found that at low power density the anode channels are blocked; while at high power density water distributed more evenly. Trabold et al. [16] used the neutron imaging technique to study the effect of the current density and cathode stoichiometric ratio on the volume of accumulated water. They reported that the amount of liquid water within the cell decreases with increasing load which indicated that a higher gas velocity is required for removing the water from the flow channels when the cell is working at the current density of $1.0 \, A \, cm^{-2}$. In addition, the effect of the cathode stoichiometric ratio on the amount of water accumulated is reported to be negligible. They concluded that the mass

transport voltage loss at higher current densities is the result of water accumulation in soft material of the cell including the GDL and MEA as opposed to the impediments in water transport in the channel. Owejan et al. [17] employed the neutron imaging technique to measure water transport through the GDL of a PEM fuel cell. They used an interdigitated flow field to force the reactant through the porous diffusion layers. The pressure differential from the inlet to the outlet was correlated to the saturation level of the GDL. The study concluded that flooding occurs primarily in the manifold at the outlet of the flow field due to pinning at the sharp transition from the channel to the manifold. In addition, they reported a significant reduction in relative permeability as the water content in the GDL reaches the critical water mass. Thus, mass transport is the limiting factor once half of the open void in the cathode GDL is full of liquid water. The neutron imaging technique was used by Turhan et al. [18] to study the effects of the reactant gas flow rates, operating cell pressures, and inlet relative humidity on the cell performance. The study showed that increasing the inlet gas flow rate significantly reduces the accumulation of liquid water in the cell. The results also suggested opposite trends for the effect of the over- and under-humidified inlet condition on the amount of liquid water in the cell. For the over-humidified inlet condition, decreasing the cell pressure increases the amount of liquid water; while for the under-humidified inlet condition the trend is reverse. Zhang et al. [19] studied the impacts of GDLs and flow fields material on formation of liquid water and its transport using the neutron imaging technique. For a serpentine flow field, they showed that the hydrophobicity of the flow field material influences the presence of liquid droplets. They also studied the influence of the GDL material on liquid accumulation on the cathode side of a quasi one-dimensional cell. It was shown that the cloth-based material generally holds less water compared to the paper-based material. They reported that a significant amount of liquid water within the GDL does not limit the electrochemical performance. In contrast, Siegel et al. [20] reported significant voltage drop due to the accumulation of liquid water on the anode side of a PEM fuel cell. They used a cell with dead-end anode and deployed neutron imaging technique to observe water accumulation. For a range of temperature, cathode inlet RH, current density and air stoichiometric ratio, they found the rate of water accumulation. The results confirmed the importance of anode flooding even when the cathode is not plugged with liquid water. Bellows et al. [21] used neutron imaging to determine the water gradient profile within the Nafion membrane. They addressed the experimental difficulties in neutron imaging by using thick membranes and careful alignment of the cell within the neutron beam. Semi-quantitative interpretation of their results suggests that the diffusivity of water in the membrane is higher than the values predicted by the models [22,23]. Using the neutron imaging technique, Hickner et al. [24] reported a lag of 100 s between the water content of the PEM fuel cell and the current density. The study also reported less water content within the cell when the working temperature is higher. For the temperature of $60 \, °C$ the study showed a peak in the water content for the current density of $650 \, mA \, cm^{-2}$. Further increase in the current density was associated with the lower water content. Owejan et al. [25] used the neutron imaging technique to obtain two-dimensional distribution of water in a cell with an active area of $50 \, cm^2$. They reported that the flow field channels with hydrophobic coating retain more water. However, the water slugs formed within the channel are smaller which improve the cell performance at high current densities. For some cases, they reported a significant difference in the cell performance when the accumulation of liquid water marginally increases. Thus, the flooding of the GDL was recognized as the primary reason for the sudden voltage drop. Kim and Mench [26] used neutron imaging to investigate the phase-

change-induced water transport mechanism in a PEM fuel cell. They recognized the gas phase as a key controlling parameter in this transport mechanism, i.e. if the gas phase exists in the catalyst layer or gas diffusion layer the phase-change-induced water transport is the dominant mechanism and the net water flux is observed from the hot to the cold region.

The principal of X-ray microtomography, also referred to as micro-computed tomography (μCT), is similar to that of the neutron imaging technique, but the static magnetic field is not necessary. The material under study scanned with X-ray and depending on the material, the X-ray beam is attenuated. An array of detectors receives the transmitted radiation from the material. By analyzing the transmitted signals the material specifications are determined. Sinha et al. [27] used this method to investigate the water saturation distribution through the GDL. They obtained the distributions along the thickness of the GDL as a function of time during the gas purging step and showed an exponential decrease in the drying rate with purge time. Manke et al. [28] employed X-ray radiography to study the evolution and transport of water inside the GDL in an in-situ experiment. They reported formation of liquid water, their growth and transport and then correlated the operating conditions to the dynamics of droplet formation. Their results suggested that the continuous GDL pore filling indicates continuous "capillary-tree-like" transport behavior which is in agreement with the results reported by Pasaogullari and Wang [29]. This eruptive transport process observed in the experiment, also directed them toward the implementation of the capillary tree patterns in their model at high current densities. Lee et al. [30] used X-ray radiography to determine quantitatively water distribution between the flow field and the GDL. They also employed an image processing technique to remove the noise of the images obtained from the radiography. A very thin cross-section of the cell including membrane sandwiched between two GDLs was investigated by Hartnig et al. [31]. The spatial and temporal resolutions in this study were 3 mm and 5s, respectively, which is quite high resolution compared to other X-ray imaging employed to investigate water transport in fuel cells. The study claims that two different diffusion barriers caused by liquid water droplets exist in the GDL when the cell is working at high current densities. The position of these barriers depends on the surface properties of the GDL, such as hydrophobicity.

The direct methods to observe flooding and water transfer in the PEM fuel cell usually requires a cell with transparent components. For instance, formation of water on the surface of the GDL as well as at the interface of the cathode gas channel is observed using direct visualization [32–42]. A microscope is usually installed and a cell with transparent flow field is used. The level of insight that these methods can provide is limited due to the opaque nature of the cell components. However, the observation of water droplet formation on the GDL surface and flow field channels is correlated to the performance of the cell if the voltage and current of the cell are measured during the experiment. Tüber et al. [32] studied cathode flooding in a small fuel cell using direct visualization. The voltage discharge performance of the cell was measured while the images of the cathode were being acquired during the operation of the cell. They reported cathode flow field blockage as a result of flooding, which impaired the performance of the cell significantly. The study reported a drop in the current density of the cell for standard and hydrophobic GDLs; while the hydrophilic GDLs showed a constant value over the first 40 min of operation. Although the paper argued better performance of the fuel cell with treated GDLs, the experiment was performed for a limited time intervals. This prevents concrete conclusion regarding the effects of hydrophobicity on the performance of GDLs in transferring water. Interestingly, the authors mentioned limited diffusivity due to more uniform distribution of water inside the hydrophilic GDL. Hakenjos et al. [33]

designed an experimental test cell to measure simultaneously the current, temperature and water distribution. They developed a segmented anode flow field for measuring the current. The back plate of the cathode flow field was made with an optical window allowing direct visualization. They used three different rates of air flow and reported its influence on the temperature and water formation and distribution. For the smallest air flow rate, the study showed that a large area of flow field is flooded with water at a low current density of 0.187 A cm^{-2}. Utilizing the current distribution, they showed that the only active area of the flow field is the inlet area. They also showed that the temperature of the flooded area was higher than the active area at the smallest air flow rate. The same pattern for temperature distribution was observed for the medium air flow rate, i.e. high temperature for flooded channels compared to the other regions of the flow field. However, the flooding region was restricted to a narrow area in the middle of the flow field. For the highest air flow rate, the active area was shifted toward the middle of the cell and the temperature distribution was almost uniform over the entire cell area.

Yang et al. [34] used a cell with a transparent cathode and explored liquid water transport at high current densities. They reported nonuniform water distribution between the channels. The emergence of liquid water droplets from preferential openings on the GDLs were studied and discussed. They highlighted the contribution of the hydrophilic flow channel in removal of liquid droplet from the hydrophobic surface of the GDL. The results identified the liquid film drainage from the gas channel as an important factor to avoid flooding in PEM fuel cells. An experimental model of an operating PEM fuel cell was developed by Borrelli et al. [35] to study the flow of water in the cathode channel. They qualitatively compared the similarities in behavior of water droplets between the model and the experimental observations reported by Tüber et al. [32]. Sugiura et al. [36] separated the gas water flow path by implementing a water absorption layer. They adopted the direct visualization technique to compare the gas flow characteristics of their design with the conventional cathode gas channels. Defining the flooding rate as the ratio of the blocked area of the channel to the area of all channels, the study showed a reduction in the flooding rate by a factor of 4 using the absorption layer. However, the polarization curve obtained for their design including the absorption layer showed a higher voltage drop at high current densities. Ge and Wang [37] adopted the direct visualization technique to investigate formation of water on the anode side. They used both serpentine and parallel patterns as the flow channels. No water droplets found on the GDL of the anode side, in contrast to the cathode side of the cell. They reported a significant effect of GDL hydrophobicity on water distribution on the anode side for the current densities smaller than 0.2 A cm^{-2}. For the hydrophobic GDL, the water is condensed on the flow channel blocking the passage of reactant gases; whereas, the hydrophilic GDL absorbs the liquid and prevents channel clogging. Although the argument is valid for the transient condition, higher saturation of GDLs is proved to reduce considerably the performance of the fuel cells. Similar to the study conducted by Borrelli et al. [35], Kumbur et al. [38] developed an experimental model to observe and study the removal of water droplets from the surface of the GDL using a direct visualization technique. They primarily studied the effect of the droplet shape and size and flow characteristics on the rate of water removal from the channels. The results showed that at the high flow rate regime (Re $\geq$ 600), the influence of PTFE loading on contact angle hysteresis is more important; while at the low flow rate on the anode side, the surface hydrophobicity has negligible effect on the instability of the droplet and hence on droplet removal. Spernjak et al. [39] examined the effectiveness of various GDL materials in water removal from the cathode flow field using

direct visualization. They visually studied the influence of the microporous layer (MPL) on water transport in the anode channel. They showed the MPL of the cathode side is responsible for formation of liquid water droplets on the anode side. They argued that the pressure gradient produced by the existence of the MPL on the cathode side diffuses the water droplet into the membrane and toward the anode side. They concluded that untreated GDLs cannot provide enough water to keep the membrane hydrated. In addition, the pores saturated with liquid water limits the transfer of reactant gases. They identified a narrow contact area between the sidewalls of the channel and the GDL as the primary area where water droplets emerge out of the GDL. In contrast, GDLs treated with the hydrophobic agent expel water in the form of discrete droplets over the entire exposed GDL/channel interface. This would leave majority of the pores available for gas transport. Using a transparent test cell, Theodorakakos et al. [40] studied droplet formation and detachment in the cathode channel. They confirmed that single-droplet detachment from the surface of the GDL is the main mechanism for water removal. They used the experimental results of direct visualization to refine and improve a numerical model developed for droplet detachment. Their study showed that an increase in the temperature helps the detachment of the liquid water droplet primarily due to reduction in liquid surface tension. The same method was used by Weng et al. [41] to study the effect of the cathode gas concentration and humidification on the performance of a PEM fuel cell. They showed that higher stoichiometric values improve the performance of the cell under humidification. For the case of non-humidified conditions membrane dehydration occurs and the cell response is not steady. They also concluded that for low stoichiometric values the change in humidification does not have a significant effect on the performance of the cell. Kimball et al. [42] studied the effect of different orientation of flow channels on the performance of the cell using direct visualization. They claimed that gravity is important and has effect on the distribution of the water droplet along the channel and the regime of liquid water flow inside the channels. The results suggested that the invasion of liquid water into the GDL requires a minimum hydrostatic pressure. Following the invasion, liquid water enters the largest available pores in the GDL and flows toward the cathode gas channel. Water droplets formed on the surface of the GDL are connected to the liquid within the GDL pores. Once the shear force in the channel is enough the droplet is detached and removed from the channel in the form of liquid slugs.

Another type of visualization method is the fluorescence microscopy technique in which the pathways of a water droplet inside the porous medium are determined by tracing the fluorescent dyes in aqueous solution. The solution is injected into the GDL sample. A UV light source excites the fluorescent dyes in the solution. The excited dyes emit light of longer wavelength, which is captured by a camera. Thus, the transport of liquid water through the GDL can be captured to the extent that the opaque fiber structure will allow. Litester et al. [2] were the group first applying the fluorescence microscopy to liquid water transport inside the GDL. They captured the images in consecutive time steps. The transient image intensity data were correlated to the height of the liquid water in the medium. The transport of liquid water through the GDL was determined using the high spatial resolution images. The physical observation of this study suggested that water transport is dominated by fingering and channeling rather than the converging capillary tree mechanism mentioned in prior work and models [43,44]. Bazylak et al. [45] employed fluorescence microscopy to study the effect of GDL compression on formation of preferential pathways for water transport. They concluded that the change in hydrophobicity due to compression of the GDL guided the travel of the liquid water through the compressed area. Alternatively,

compression may cause damage to the porous structure of the medium, which results in formation of macroscopic cracks in the sample. These cracks may be chosen by water as the preferential pathways since their corresponding radii are much higher than the actual pore size of the medium. Thus, water would face less resistance and flow through the compressed region. Using scanning electron microscopy (SEM) the morphology of the samples was also studied after compression. The breakup of fibers was reported as well as deterioration of the hydrophobic coating. In their next work, Bazylak et al. [46] studied dynamic water transport and emergence of droplets through the GDL. The study showed that droplets emerge from the GDL at preferential breakthrough locations. The locations of the breakthrough change periodically. Thus, the water pathways within the GDL are dynamically interconnected. The same group used a fluorescence technique to study the interaction of the water droplet with a solid wall on a hydrophobic gas diffusion layer [47]. The effect of plate surface properties on the droplet's stability was investigated. The study proposed the use of hydrophobic land areas (at the GDL/land interface) as the channel hydrophobicity enhances the mitigation of the accumulated water droplet under the land area to the gas flow channel.

1.2. Pore-network modeling

In the capillary-controlled displacement process which occurs in the GDLs, the viscous forces are not dominant. Due to the small values of capillary number ($Ca = \mu V/\sigma$, representing the relative effect of viscous forces versus surface tension), the random and invasion-percolation models appear to be the proper approach toward the modeling of such displacements. However, the predictive properties of these models are limited to very simple systems and most of the studies are concentrated on two-phase flow in water-wet media. The earliest pore-network model was developed by Singhal and Somerton [48] followed by Mohanty et al. [49] and Payatakes et al. [50]. Mohanty et al. [49] simulated both low and high Ca regimes in a square network of pores. They modeled the imbibition process and investigated the effects of pore and throat size distribution on the flow configuration [49]. In the 1980s, the pore-network models were used for more detailed systems [50–54]. Lenormand and Zacone [55] extensively used pore-network modeling to study immiscible two-phase displacement in porous media. Nam and Kaviany [43] were the first to implement a pore-network model to gas diffusion layers. They assumed that intersecting fibers surrounded the void volume of the pore body. These intersecting fibers overlapped on each so that the solid matrix of the medium was modeled by stacks of these fibrous structures. By changing the position of the fibrous layers, the whole porous medium was reconstructed making the coordination number to be 8. The model enabled the study of formation and distribution of condensed water in the GDL and its tendency to reduce the local effective mass diffusivity. In essence, the local effective mass diffusivity of the fibrous diffusion medium was determined as a function of the local porosity and local water saturation. Using this in conjunction with the hydrodynamics of capillary, two-phase flow in a hydrophobic porous medium as well as the water formation rate (hydrogen−oxygen reaction), condensation kinetics, and one-dimensional distribution of water saturation was determined. They also studied the role of the fiber diameter, porosity, and capillary pressure on the cell performance using the network model. These results were then used to develop a two-layer diffusion medium for the enhancement of the cell performance.

Gostick et al. [56] implemented a pore-network model to compute the relative permeability of water and gas and the effective gas diffusivity as a function of water saturation using the resistor network theory. The model was primarily designed to estimate the

multiphase flow and properties of the GDL. Based on two commonly used GDL materials, the model was calibrated by adjusting its parameters to match the experimental data, especially the absolute permeability as well as the capillary pressure curves for the drainage process. By implementing the boundary conditions of a working fuel cell and physical parameters on the network model, limiting current calculations were performed. This limiting current was calculated for different levels of water saturations in a section of the GDL. Half of this section was open to the gas flow channel and the other half was covered by the land. Similar to previous study [43], Gostick et al. [56] calculated the effective diffusivity as a function of porosity and water saturation (s). The relative effective diffusivity and relative permeability were correlated to the saturation with different suggested exponents in the form of s^a. No experimental results were reported to verify the above correlation.

Sinha and Wang [57] used a quasi-static approach to model the immiscible displacement of liquid water inside the GDL. They studied dynamics of water transport at the pore-level and obtained profiles of water saturation in the GDL while the fuel cell was operating in realistic conditions. They reported that the controlling force in transporting liquid water in the GDL is the capillary force, and water flows through the connected clusters with finger-like frontiers. They also reported the influence of the GDL–channel interface covered by liquid water on the transport mechanisms inside the GDL. In their following paper, Sinha and Wang [58] considered a GDL with mixed-wettability properties. The effect of wettability distribution on the transport mechanism of liquid water was studied using a pore-network model. The GDL modeled in this study was assumed to be used in a fuel cell at realistic operating conditions. The study showed that for the mixed-wet GDL water transports through the network of hydrophilic pores avoiding the finger-like configuration which occurs in the hydrophobic GDL samples. However, the model does not consider any saturation for each pore. As a result, the invaded pore is filled immediately as the water finds a way to get through; whereas, the saturation of the pore occurs gradually in progressive time steps.

Chapuis et al. [59] combined pore-network simulations and visualizations obtained from transparent micromodels to study two-phase flow dominated by the capillary effects. Using a Voronoi diagram, they developed a pore-network model by assigning particular sections of the diagram to pores, bonds (throats) and disks (which represents the fibrous structure). It was shown that the process of liquid water invasion in a hydrophobic medium can be simulated using the classical invasion-percolation algorithm provided that the contact angle is much smaller than 90°. For contact angles near 90°, the mechanisms for the local growth of the interface affect the invasion pattern. It was also shown that the invasion pattern is dramatically different in a hydrophilic medium.

Markicevic and Djilali [60] employed a pore-network model with trapping algorithm to study multiphase flow in porous media. They used a 2D regular network with varying diameter for the throat. They also assumed that only one phase can invade a particular throat. The throat radii were determined with respect to experimental measurements obtained for permeability (K) and capillary pressure (P_c). From the model, they determined a length scale (l_s) representing the onset of phase invasion into the next fraction of the network. The length scale (l_s) seems to be a function of flow regimes: for the viscous dominant regime, l_s is less than that of the capillary dominant regime. This suggests that the invasion process occurs more frequently in the viscous dominant regime leading to higher saturation and lower relative permeability. For each phase, two different saturations (mobile (s_i) and immobile ($s_{im,i}$)) were defined, and momentum was transferred between phases through the mobile clusters. Thus, phase saturations were defined with respect to the mobility of the phases. For invasion of

one phase to the other, the pressure of the invading phase should be higher than the second phase and the capillary pressure of the connecting throat (P_c), which is defined using the Young–Laplace equation. The phase pressure was calculated using the conductance of the throats and the conservation of mass for every pore. The flow in each throat was also calculated using the Poiseuille law. Once the pressure distribution was determined the flow rate was calculated by summing the flow rates through the throats at the inlet and outlet boundaries. The permeability for each phase was then determined using Darcy's law [61]. Finally the capillary pressure (p_c) was found by averaging the local capillary pressures over the interface at the termination points. Using this algorithm, a two-phase flow in a gas diffusion layer was investigated. The Relative permeability and capillary pressure as a function of the phase saturation were obtained, and general flow configuration was studied. Markicevic and Djilali [60] suggested that the relative permeabilities follow a power law of saturation. The sensitivity analysis showed that the permeability of the invaded phase changes drastically with the saturation of the invaded phase compared to that of the invading phase. In addition, the numerical results suggested that the exponent is a stronger function of the cluster size than the medium heterogeneity. Thus, the capillary pressure marginally changes by varying the saturations while it significantly varies as the cluster size and the heterogeneity of the medium change. The cluster size also influences phases' percolation: phase channeling occurs for small clusters. The possible problem of this approach is the application of a 2D network for simulation of two-phase flow in the GDL. Although the assumptions made in the study reasonably predicted the configuration of flow and fluid fronts, they made the algorithm very complicated and difficult to comprehend. In addition, there is lack of physical evidence in validating the assumptions used in the algorithm (e.g. the length scale (l_s) being a function of the flow regime).

Kuttanikkad et al. [62] studied the effect of hydrophobicity on water flow in the GDL using a pore-network model. The study used a regular 3D network of cubical pore interconnected with ducts presenting the throats. An average pore diameter of $d_p = 17.5$ µm on a $40 \times 40 \times 10$ network was distributed. All the pores and throats were also considered as elements which can be either hydrophobic or hydrophilic. In order to incorporate the effect of hydrophobicity, a portion of the pores and throats $(1 - f)$ was considered as hydrophobic portion by assigning the contact angle of 115°. For the remaining fraction (f) the contact angle was assumed around 80° presenting the hydrophilic property of the GDL sample. Thus, each element (i.e., pore or throat) attributes a threshold pressure which is a function of the element geometry (radius of the throat and pore), interfacial properties of the element (contact angle (θ) and surface tension (σ)) and an adjusting pressure determined with respect to hydrophobicity of the medium to reflect the experimental measurement. The pore radii (r_n) used to evaluate the pore threshold pressure were calculated with respect to the initial pore size distribution and the status of the surrounding throats. For instance, the pores are larger if the surrounding throats are already invaded and smaller if the throats are not wetted yet. This would increase the chance of invasion of the pore if the surrounding throats were wet. The model was then implemented to different hydrophilic fractions (f) and showed that the capillary pressure–saturation curves are identical for these cases when the liquid saturation is low (less than 50%). For higher saturation, the curves reproduce the results obtained experimentally [63]. In order to estimate the relative permeability values, arbitrary pressure values were imposed as boundary conditions at the inlet and outlet of the network (P_{inlet} and P_{outlet}). Then, the total flow rate (Q) over the entire network was calculated using the pore-network model. Following this, Darcy's law was used to determine the permeability.

The results show that at low liquid saturation, the relative permeabilities are almost identical for all the hydrophilic fractions (f). For intermediate values of the saturation (around 0.5), the gaseous phase relative permeability increases slightly with the fraction of hydrophilic pores; whereas the opposite behavior was observed for the liquid water relative permeability. For low saturated GDL samples (lower than the percolation threshold, f_c), they concluded that the macroscopic properties of the medium such as permeability, capillary pressure and saturation are independent of the hydrophobicity of the medium.

El Hannach et al. [64] compared two different pore-network algorithms to study liquid water transport in the cathode catalyst layer (CCL) of the PEM fuel cell. The study assumed the CCL to be made of spherical agglomerates of the carbon support and platinum particles. Water was assumed to be produced within these agglomerates. In the pore-network model, the void space in between the pores and throats was considered to be filled with the agglomerates. Water was injected into the network through the randomly distributed "active" agglomerates within the network. All the network components (pores and throats) were evenly open to water injection. The criteria for the invasion followed the same procedure described in Refs. [62], i.e. the pore diameters were enlarged if the adjacent pores/throats were filled with water as proposed in Refs. [61,65]. The study shows that liquid water configuration follows the fingering regime and stable displacement ("fist-like" configuration) in the hydrophobic and hydrophilic media, respectively. Thus, for the hydrophobic medium the fingers grow independently making the total saturation higher compared to the hydrophilic medium. It also shows that water enters the gas diffusion layer through a series of independent injection points, corresponding to the CCL breakthrough points. In contrary to the study performed by the same group [62] which concluded that the effect of GDL hydrophobicity is negligible at low saturation, El Hannach et al. [64] show that wettability has significant influence on water transport in the catalyst layer.

Recently, Pauchet et al. [66] studied the effect of GDL hydrophobicity degradation on the performance of the PEM fuel cell using a pore-network model [66]. They argued that the loss of hydrophobicity in the GDL can explain the performance loss during the life span of the PEM fuel cell. Similar to the algorithm implemented in Ref. [62], they simulated the loss of hydrophobicity by increasing the fraction, f, of the hydrophilic pores. As the hydrophilic fraction (f) value approaches the percolation threshold (f_c) value the effective gas diffusion coefficient drops significantly which induces a decrease in the cell potential.

Kang et al. [67] developed a "similarity model experiment" to simulate the flow of a non-wetting fluid through a porous medium with the same dimensionless numbers as in a working PEM fuel cell. A physical domain of 30 cm × 30 cm × 7.2 cm was modeled with uniform flux injection through a disk with diameter of 10 cm. The invasion-percolation path finding procedure developed by Lee et al. [68] was used to determine the saturation distribution of the non-wetting fluid in the steady-state condition. The algorithm sought the transport pathways with the lowest values for the entry pressure. The procedure starts from the pores at the inlet which were occupied by the non-wetting phase. The results of the visualization showed that an intermediate layer sandwiched between a fine and a coarse layer delays the process of capillary fingering in the coarse layer, which reduces the volume of the non-wetting fluid. The pore-network developed in this study measured the total volume of non-wetting fluid injected into the porous medium. The modeling results are in close agreement with the experimental results.

Wu et al. [69] developed a pore-network model based on the invasion-percolation algorithm to study transport of liquid water and reactant gas transport through the GDL. The average diameter and

length of the throat in this model are considered to be 9 μm and 25 μm, respectively, within a 80 × 80 × 12 network size. The network was initially considered to be completely hydrophilic, and then a fraction $(1 − f)$ of the pores were rendered into hydrophobic pores by randomly assigning a constant contact angle of $\theta = 110°$. The invasion process followed a sequential procedure, in which a number of inlet throats are the injection points. In this procedure, liquid invasion from the first injection point is conducted until breakthrough. Then, the invasion process for the second injection point is performed, and so on. The study concludes that the liquid water is evenly distributed along the GDL thickness for low hydrophilic fractions ($f \leq 0.2$). It is also shown that the hydrophobicity does not have any influence on the limiting current of the cell when the number of injection points is low (which simulates the low current density condition). At higher current densities, however, the simulation shows that the limiting current is not changing monotonically with hydrophobicity, and hence there is an optimal PTFE loading leading to the best fuel cell performance. The same group investigated the transport and reaction process in the cathode catalyst layer (CCL) using a pore-network model [70]. The catalyst layer was assumed to have primary pores (as the agglomerates) and secondary pores (as the void space within the catalyst layer). Thus, the model only considers the secondary pores to simulate the reaction and transport phenomena. The length and average diameter of the throats were assumed to be 100 nm and 55.7 μm, respectively. A 15 × 15 × 100 network was constructed corresponding to the 10 μm-thick catalyst layer. The oxygen concentration and the reaction rate profiles along the CCL thickness were predicted using the model.

In this paper fluorescence microscopy is adopted and the details of water flow inside the GDL are captured, analyzed and studied in details. The main characteristics of water flow in the GDL derived from the experimental investigation are categorized into three patterns: invasion, progression and pore filling. The characteristics are used to develop a pore-network model. The developed model is applied to GDL samples with different hydrophobic fractions to investigate the effect of hydrophobicity on the flow configuration at breakthrough.

2. Experimental

2.1. The setup

The details of the setup components are presented in Fig. 1(a). For each experiment, a fresh Toray GDL sample (TGP-H-30 with 0% or 40%wt PTFE loading, Toray International, Inc., Chuo-ku, Tokyo, Japan) is placed in the injection channel. The fluorescein solution is pumped into the sample from the bottom surface with the flow rate of 1.11×10^{-11} m³ s⁻¹, corresponding to the flooding condition (see Appendix A which includes the detailed calculation of this flow rate). Through the microscope, the CCD camera captures the images of water flow inside the GDL in incremental time steps. The signals sent from the camera, micro-needles and the pressure transducer are transferred to the PC and saved for future analysis. The injection channel is fabricated from a PTFE rod (ASTM D 1710) to prevent any unwanted leakage in the gap between the GDL sample and the surface of the injection channel. The detailed schematic of the injection channel is shown in Fig. 1(b). The channel is composed of a 3.3 mm diameter vertical hole drilled through a PTFE rod and four horizontal holes with diameter of 300 μm. Four needles are installed in the horizontal holes. The first needle applies voltage to the aqueous solution inside the channel, while the other needles act as voltage sensors. By measuring the time sequence of signals provided by the sensors, and knowing the distance between the needles, the flow rate is measured. The measured flow rate is then compared with the flow rate provided
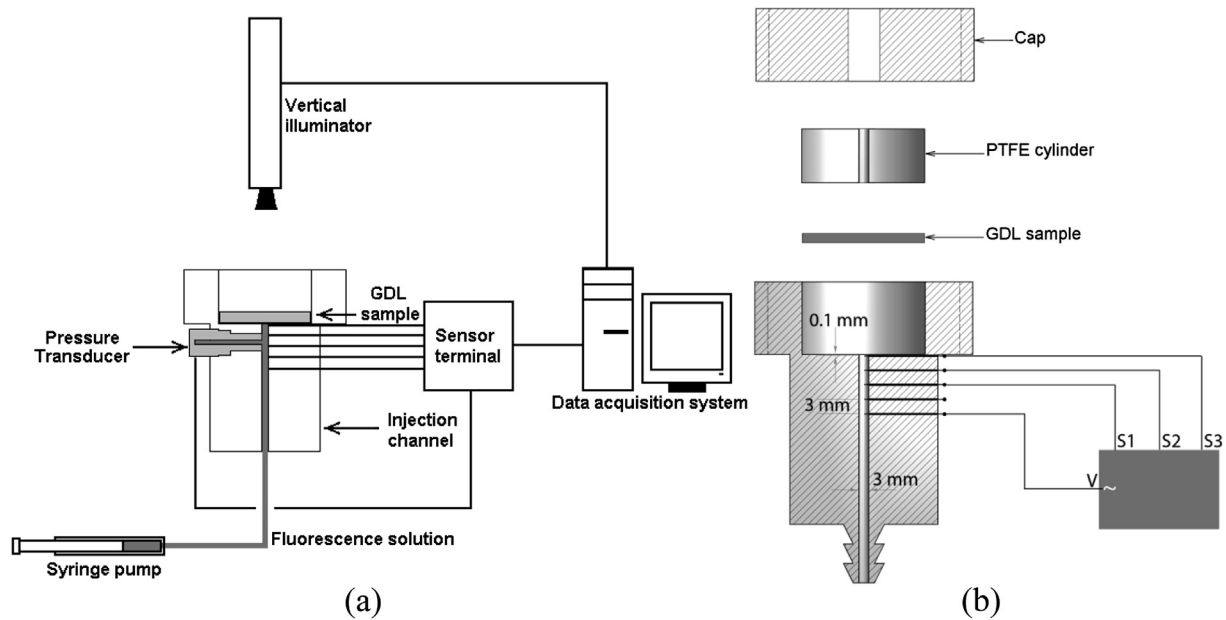
Fig. 1. Schematic of (a) experimental setup, and (b) injection channel.

by the syringe pump in order to detect any possible leakage in the injection module (tubing, syringe and the channel). The surface of the channel is treated with a very thin layer of poly-dimethylsiloxane (PDMS). In addition to the extra hydrophobicity which PDMS provides, its flexibility prevents the GDL sample from breaking under the pressure imposed by the PTFE cylinder and the channel surface. However, the PDMS layer needs to be replaced after each experimental run, due to its deterioration after exposure to the fluorescein solution.

2.2. Fluorescence microscopy

The fluorescence vertical illuminator includes a reflected light microscope. In this microscope, the wavelength of the excitation light is shorter than the wavelength of the reflected light. An arc-discharge lamp produces multispectral light, which passes through a wavelength selective excitation filter [71]. Wavelengths passed by the excitation filter reflect from the surface of a dichroic mirror, through the microscope objective to bath the specimen with intense light. The emitted light from the fluoresced specimen is gathered by the objective lens and is passed through the dichroic mirror. A barrier filter blocks any residual excitation wavelengths and only allows the longer emitted wavelength to pass through, and these filtered wavelengths are finally captured by a CCD camera. The specifications of the fluorescence microscope used in this study are described in the following section.

The UV light source (EXFO X-Cite120Q Mercury halide short arc) provides an ultraviolet light beam with the wavelength in the range of 400–600 nm. The light wave passes through an excitation filter (490 nm) inside the illuminator. Reflected from the dichroic mirror, the shortwave light baths the GDL sample and excites the fluorescent dyes in the solution. The emitted light passes through the dichroic mirror and the barrier filter (550 nm) and captured by the CCD camera (DFC 340 FX). The vertical illuminator is basically an APO Zoom microscope with a photo tube (HC L 2TU 1.25X). The magnification of the main objective lens is 1.0×, and the C-Mount adapter also provides 0.55× zoom. The field of view is a window of 3.3 mm × 3.3 mm. The total magnification is 25× and the numerical aperture (NA) is 0.049, which makes the depth of field around 0.392 mm. This ensures that the entire thickness of the GDL is in focus while the liquid is flowing inside and images are captured. The lateral resolution is 6.8 μm and the time interval between two consecutive images is 1 s. Since the fluorescent dyes are extremely bright compared to the black background of the image (the fibrous material of the GDL), the time of exposure must be optimized. For the long exposure time the image will be bleached out; whereas for a short exposure time the low intensity spots (presenting locations with the lower fluorescence concentration) might not be appropriately captured. The optimum exposure time for the experiments was set as 10.9 ms (Fig. 2).

3. Numerical

3.1. The network

A typical porous medium consists of two sections: (1) the solid matrix, which is the physical material of the porous medium (i.e.
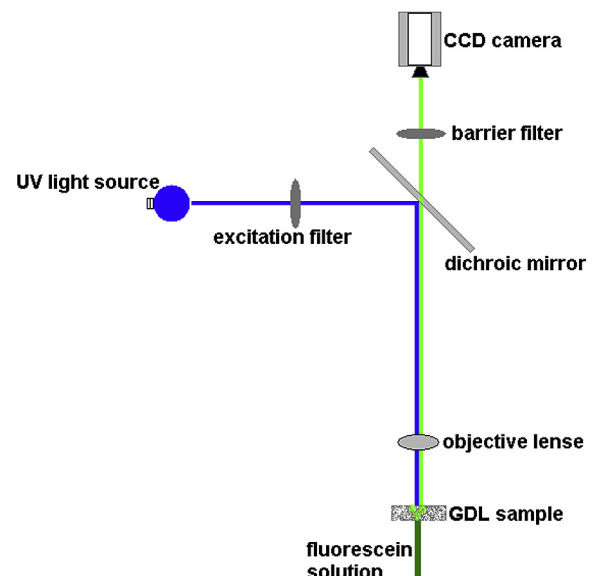

Fig. 2. Schematic of fluorescence microscopy technique.

carbon fibers in the GDL) and (2) the void space in between the solid matrix, which is called the pore body. The pore body withholds the fluid injected or fed into the medium. The boundary between two adjacent pores is called the throat, in which the pressure drop occurs. In a regular 3D pore-network, each cell is connected to six adjacent cells (presenting the coordination number). Fig. 3(a) shows a typical cell with its adjacent cells and the corresponding index notations. The entire network is presented in Fig. 3(b). The *x-y* planes correspond to the interface of the GDL-catalyst layer and the planes parallel to that. The *z*-direction is along the GDL thickness. The liquid water is injected through the GDL from the *z = 0* plane.

The cell is a representation of the physical void volume in the porous medium (pore body). The dimensions of the pores are determined using the porosimetry data reported in Ref. [72]. In this study, the diameter is randomly assigned in the range of $10 \, \mu m < d_{pore} < 20 \, \mu m$. The pore body withholds the fluid inside the porous medium, and the interface of the adjacent pores is where the pressure drop occurs. Similarly, in the simulation, the accumulation of fluid in the porous medium occurs inside the cells and all the pressure variations occur in the throats. Thus, the dimensions of the throats are determined based on the pressure drop in the medium and the thickness of the medium. The length of throat is $l_{throat} = 11 \, \mu m$, and its diameter is randomly distributed in the range of $5 \, \mu m < d_{throat} < 10 \, \mu m$. The number of cells in the *z*-direction (*KMAX*) is determined based on the thickness of the GDL sample. For the samples with the thickness of 110 μm, *KMAX* = 10. For a disk of diameter of 3.3 mm, the injection flow rate of $1.11 \times 10^{-11} \, m^3 \, s^{-1}$ is used to mimic the mass flow rate at the flooding condition. If the same area is used for simulation, a 150×150 network should be adopted, which is computationally expensive. Thus, the exposed area is reduced by a factor of 100, which results in a 15×15 network. To ensure the validity of the simulation, the total flow rates of liquid water injected into each sample were analyzed against the exposed area. Fig. 4 shows the initial flow rates at the onset of simulations versus the exposed area for different networks. The figure shows the injection flow rate is 100 times less than the experimental condition as the exposed area in the numerical simulation is reduced by the same factor.

Commercial gas diffusion layers (GDLs) are treated with a hydrophobic agent (PTFE). It has been shown [73–78] that the performance of the cell working with treated GDLs is better in terms of water management. The hydrophobic agent partially covers the pores in the medium. As a result of this coverage, the hydrophobic pores are less vulnerable to water invasion. Thus, a series of connected hydrophobic pores can produce a passage for the reactant gases to be transferred from the gas channel to the catalyst layer.
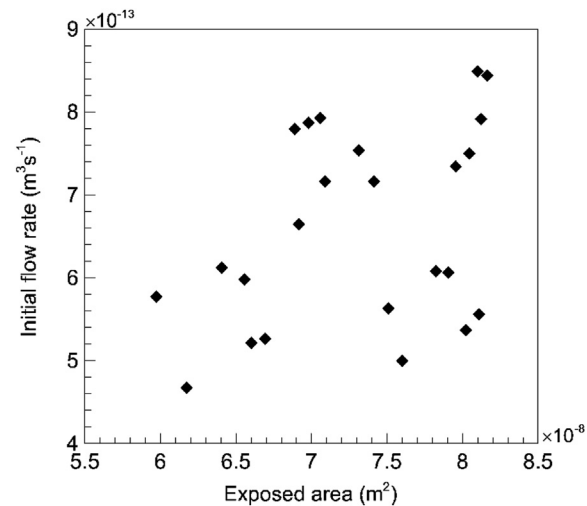

Fig. 4. Initial flow rate versus total exposed area.

The difference between an untreated and treated GDL might not be significant while the fuel cell is working at low current densities (smaller than the current associated with flooding). However, at high current densities where the mass transport losses become dominant, treated GDLs perform better [1]. To implement the effect of hydrophobicity of the GDL sample in the simulation, the contact angle values are assigned to the pores in the network. First, the network is considered as a hydrophilic medium as the contact angle of the solid matrix (carbon fibers) is less than 90° [79]. Therefore, a random distribution of contact angle values in the range of $60° < \theta < 90°$ is assigned to all of the pores to present the interfacial properties of the solid matrix. Then, based on the hydrophobic fraction of the GDL sample, the number of pores required to be modified is calculated. The details of this calculation are summarized in Appendix B. Subsequently, the contact angle of these pores are modified randomly between $90° < \theta < 120°$. Fig. 5 shows the treated networks used in this study. The blue and red spheres represent the hydrophilic and hydrophobic pores, respectively. The properties of the networks and the fluids are summarized in Table 1.

3.2. Displacing algorithm

The pore-network modeling approach is used to study the transient flow of fluid through the porous medium. The simulation is focused on the flow of water inside the GDL from the start of
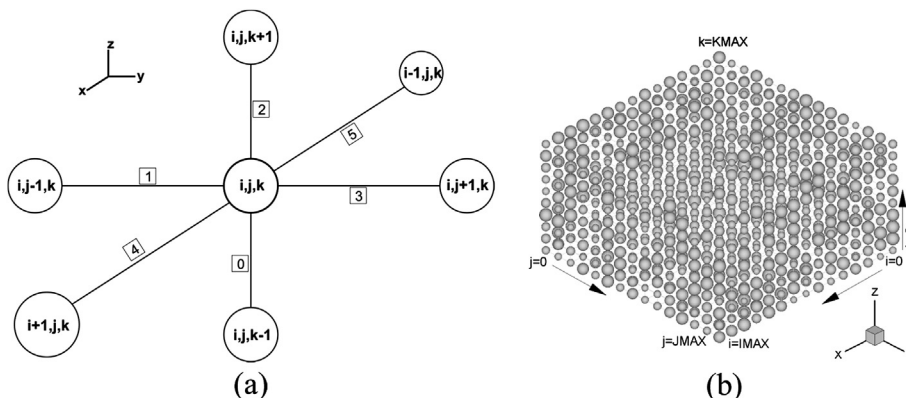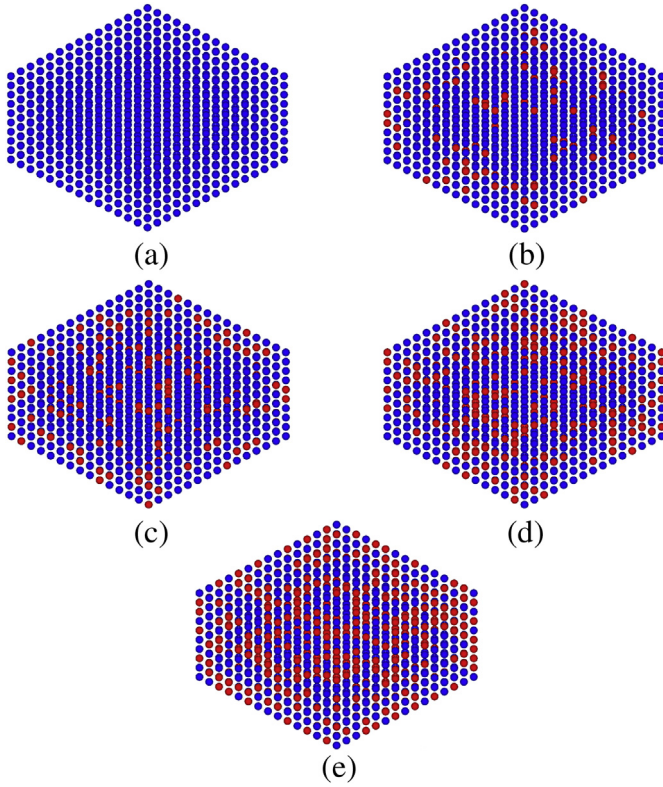

Fig. 3. Schematic of (a) cells representing the pore body, and (b) a sample of pore-network structure.

Fig. 5. Treatment of network with hydrophobic fractions of (a) 0%, (b) 10%, (c) 20%, (d) 30%, and (e) 40%.

injection of the fluid into the medium up to the breakthrough (identical to the experimental conditions). The data collected in the experimental section is used for modifying the model and setting the boundary condition. In particular, the measured pressure values are employed as the boundary condition. The first row of the network (plane $z = 0$) is the catalyst layer. It is assumed that all the surface of the catalyst layer is active at the condition of flooding. Thus, all the cells of this row are filled with pressurized liquid water. The values of the pressure for the untreated sample and the sample with 40% PTFE loading are considered as 5318.6 Pa and 7041.7 Pa, respectively, measured experimentally. The pressure boundary conditions for the remaining samples with 10%, 20% and 30% PTFE loadings are interpolated using the experimental values obtained for 0% and 40% samples. During the simulation, these cells remain filled with water and provide water to the entire network. The saturation of these cells which is defined as the ratio of the fluid volume within the cell to the total volume of the cell ($S_{cell} = V_{fluid}/$

Table 1
Properties of the network and fluids.

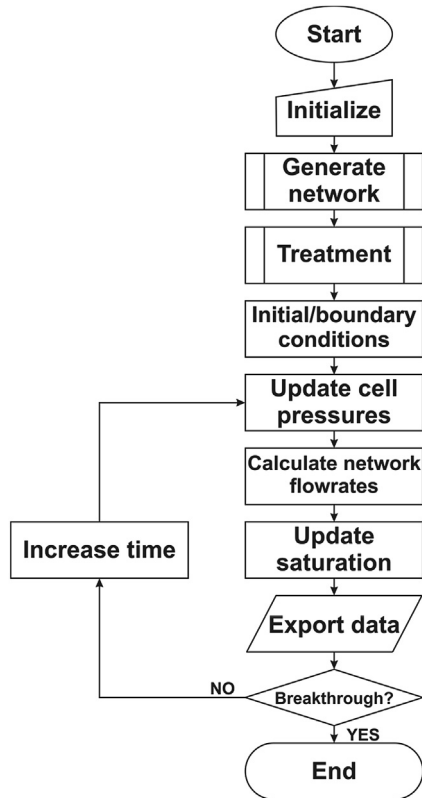| Variable	Value
Network size	$15 \times 15 \times 10$
Coordination number	6
Pore diameter (d_{pore})	10—20 μm
Throat diameter (d_{throat})	5—10 μm
Throat length (l_{throat})	11 μm
Water viscosity (μ_w)	1.002×10^{-3} N m^{-2}
Water density (ρ_w)	1000 kg m^{-3}
Surface tension (σ)	0.072 Nm^{-1}
Air viscosity (μ_{nw})	1.85×10^{-5} N m^{-2}
Air density (ρ_{nw})	1.190 kg m^{-3}
Contact angle range (hydrophilic)	60—90°
Contact angle range (hydrophobic)	90—120°

V_{cell}) remains constant during the simulation ($S_{cell} = 1$). Fluid inside a cell invades the adjacent cells if the following two criteria are met: (1) the fluid pressure in the invading cell is high enough to overcome the capillary pressure of the connecting throat and, (2) the pressure difference between the cells is high enough to overcome the resistance due to friction in the throat. The first criterion considers and deploys the surface properties of the medium. The significance of the capillary-driven flow inside the porous medium is observed in this term:

$$P_{liquid} - P_{gas} > P_{capillary} \tag{1}$$

in which $P_{capillary}$ is determined with respect to the diameter of the throat and surface properties of fluid using Young—Laplace equation

$$\Delta P = \sigma \left(\frac{1}{R_1} + \frac{1}{R_2} \right) \tag{2}$$

where ΔP is the pressure difference across the fluid interface, σ is the surface tension of the fluid, and R_1 and R_2 are the principal radii of curvature. For a circular tube with a diameter of d, the Young—Laplace equation can be simplified to

$$\Delta P = \frac{4\sigma \cos \theta}{d} \tag{3}$$

in which θ is the contact angle between the fluid and the medium. The frictional resistance of the throat is estimated using the Poiseuille equation for laminar flows

$$\Delta P = \frac{128 \, \mu L \, Q}{\pi d^4} \tag{4}$$

where ΔP is the pressure gradient at two ends of the throat, μ is the dynamic viscosity of the moving fluid, Q is the flow rate of the fluid and d is the diameter of the throat. The pressure of each cell includes two terms as shown in Eq. (5): (i) the hydrodynamic term which is a function of local saturation (S_{cell}) and the reference pressure (the pressure at the boundary), and (ii) the capillary term which depends on the contact angle and the diameters of the throat connected to the cell.

$$P_{cell} = P_{hydrodynamic} + P_{capillary} \tag{5}$$

The hydrodynamic term ($P_{hydrodynamic}$) is zero or has a positive value for the cases where liquid is injected into the sample ($P_{ref} > 0$). If no fluid exists in the cell ($S_{cell} = 0$), the hydrodynamic term is zero. The capillary term ($P_{capillary}$) is a function of fluid contact angle (θ). For the hydrophilic cells, where $\cos \theta > 0$, the capillary term is positive. This implies that the capillary is a driving force for hydrophilic pores, contributing to the total pressure of the cell. For the hydrophobic cell, on the other hand, the capillary term is negative ($\cos \theta < 0$), reducing the total cell pressure, P_{cell}. Either term ($P_{hydrodynamic}$ or $P_{capillary}$) can be the dominant depending on the condition of the flow and the regime under study. At a high capillary number ($Ca = \mu V/\sigma$), the viscous force can be dominant over the surface tension. Similarly in the simulation, the capillary term is negligible and the share of the hydrodynamic term in the total pressure of the cell is higher. At low capillary number, on the other hand, the surface tension force dominates and affects the flow configuration.

Fig. 6 summarized the displacing algorithm used in this study. In each time step, the cell pressure (P_{cell}) is estimated for each throat connected to the cell using Eq. (5). In fact, the cell has six pressures for every six directions as shown in Fig. 3(a). Thus, every throat has

Fig. 6. Flowchart of the displacing algorithm.

The calculated flow rates in each throat are used to update the volume of the fluid in each cell. Thus,

$$V_{\text{fluid},t} = V_{\text{fluid},t-1} + \sum_{i=0}^{5} Q_{\text{throat},i} \times \Delta t \qquad (7)$$

where, $V_{\text{fluid},t}$ and $V_{\text{fluid},t-1}$ are the volume of the fluid at time t and $t-1$, respectively. The saturation of each cell is estimated as

$$S_{\text{cell}} = \frac{V_{\text{fluid}}}{V_{\text{cell}}} \qquad (8)$$

Using the cell saturation (S_{cell}), the hydrodynamic pressure of each cell is updated based on

$$P_{\text{hydrodynamic}} = S_{\text{cell}} \times P_{\text{ref}} \qquad (9)$$

Then, the total pressure of the cell is updated using Eq. (5). The updated cell pressures are used to calculate the flow rate of each throat in the next time step. In each time step, the saturation and pressure fields are estimated for the entire domain (network of pores). The algorithm stops when the condition of breakthrough is achieved. Breakthrough is defined when the pressure of at least one of the cells in the last row is equal to the breakthrough pressure measured experimentally.

4. Results and discussion

4.1. Imaging

For the treated and untreated samples, four consecutive images of water flow through the GDL are presented in Figs. 7 and 8. The color mapping of contours provided for each image is correlated to the light intensity of the pixels in the real image, i.e. the areas colored in red represent the pixels with more intense fluorescence emission. (For interpretation of the references to color in these figures, the reader is referred to the web version of this article.)

Litster et al. [2] correlated the intensity of pixels to the height of liquid water in through-plane direction. However, the concentration of fluorescent dyes in a particular pore in the GDL affects the intensity of light emitted from the pore. For a fully saturated pore,
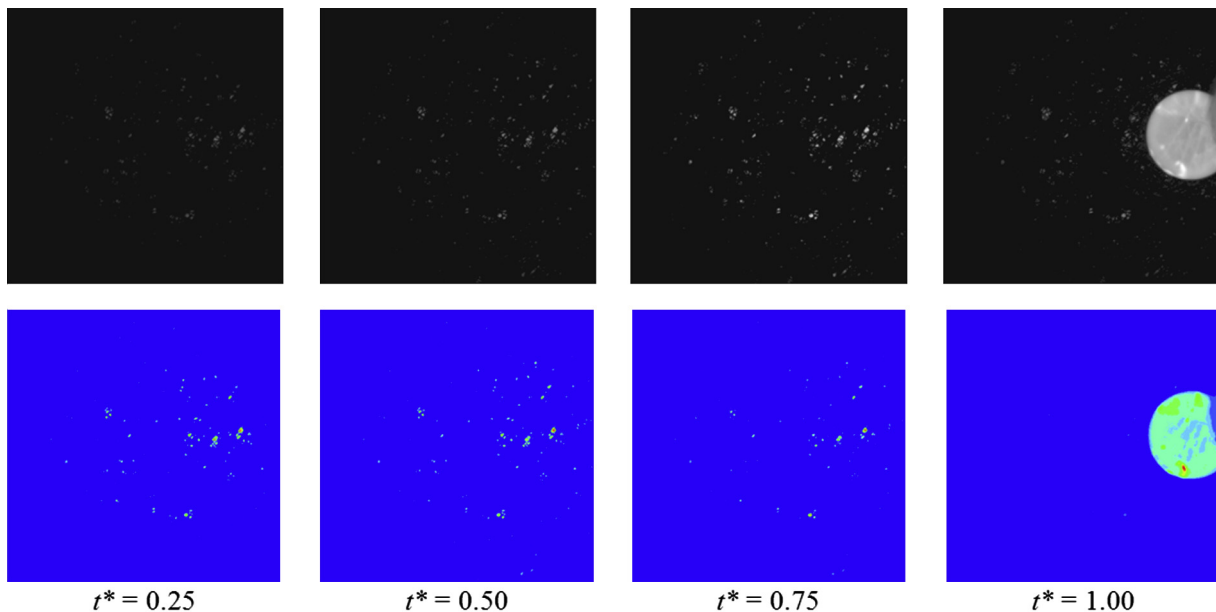
two pressures at the two ends which correspond to the cells attached to it. Using Eq. (4), the flow rate of the throat is calculated by

$$Q_{\text{throat}} = \frac{\pi d^4}{128\,\mu l_{\text{throat}}} \left(P_{\text{cell},1} - P_{\text{cell},2} \right) \qquad (6)$$

$t* = 0.25 \qquad t* = 0.50 \qquad t* = 0.75 \qquad t* = 1.00$

Fig. 7. Evolution of water through the GDL (untreated sample).

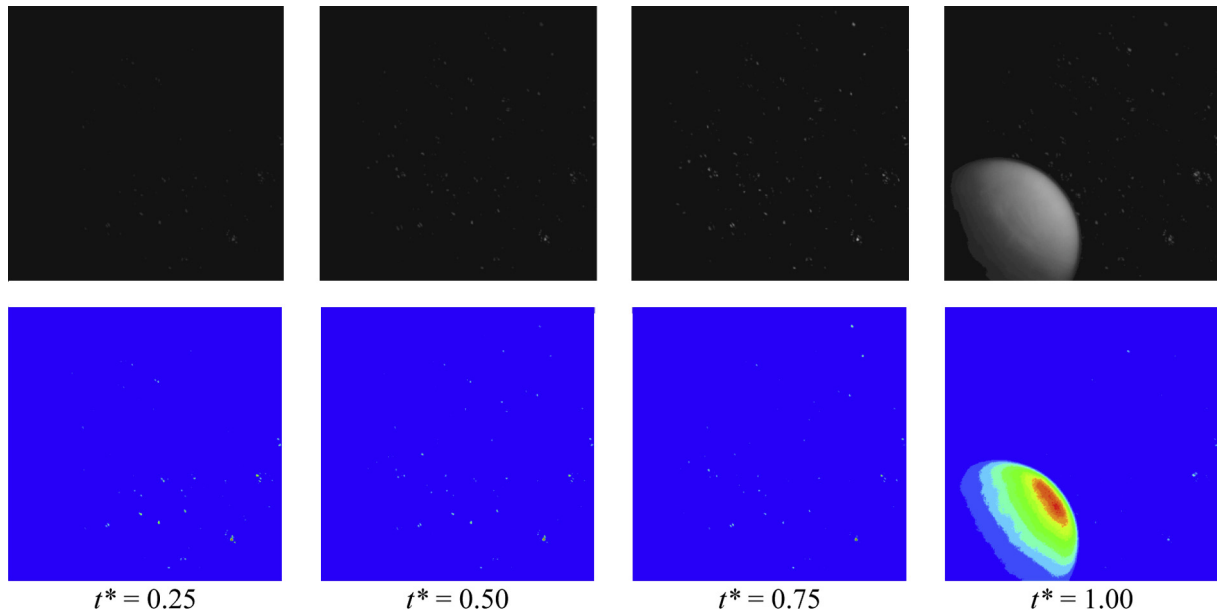$t^* = 0.25$ $\qquad\qquad$ $t^* = 0.50$ $\qquad\qquad$ $t^* = 0.75$ $\qquad\qquad$ $t^* = 1.00$

Fig. 8. Evolution of water through the GDL (treated sample).

the intensity of the dye shows the pore brighter than a partially filled pore. Thus, the saturated pore is recognized with red-color mapping in the contours while the empty pores remain blue. The correlation between the image intensity and the pore saturation is used in the following section to study the flow characteristics for the treated and untreated GDL samples.

4.2. Flow characteristics

In this section, the images of water flow inside the porous medium of the GDL is presented, analyzed and discussed. Although not all the active area and thickness of the GDL is visible in fluorescence microscopy due to opaque nature of carbon fibers, the images provide basic insight into important phenomena occurring during water flow through the GDL. Qualitative analysis of images obtained from this technique helps to understand the hydrodynamics of flow which eventually leads to a more accurate model for liquid flow inside the porous medium. Based on the results, a numerical pore-network model is developed and presented. The critical concepts and criteria used in the model (e.g. pore saturation, invading criteria, and hydrodynamic pressure term) are derived based on the observation and analysis of flow configuration, and the measurement of flow characteristics discussed in this section. The presented images are for a fuel cell working at flooding condition (which is equivalent to the injection flow rate of $1.11 \times 10^{-11} \text{ m}^3 \text{ s}^{-1}$).

4.2.1. Initial invasion pattern

Water invades the pores quite differently in a hydrophilic medium compared to a hydrophobic medium. In a hydrophilic medium, the majority of pores are available to be invaded by liquid water due to distribution of the local contact angle for each pore. In a hydrophobic medium, on the other hand, the pores are less vulnerable to water invasion. For two-phase flow in porous media, the capillary pressure is defined as the pressure difference between the phases. In the case of the GDL, water is the invading (or displacing) phase and air is the invaded (or displaced) phase. The Young–Laplace equation correlates the capillary pressure to the

hydrodynamic and geometrical properties of the porous medium (Eq. (3)). For a drainage process to occur inside the GDL, the liquid pressure should be high enough to overcome the pore capillary pressure

$$P_{\text{liquid}} - P_{\text{gas}} > \frac{4\sigma\cos\theta}{d} \qquad (10)$$

When a GDL is treated with a hydrophobic agent (PTFE), the local contact angle of pores changes. Thus, the liquid pressure should increase to overcome the resistance of the pore and make the water droplet invade it. In addition, less numbers of pores are vulnerable to invasion by water in a hydrophobic medium; whereas in a hydrophilic medium, the number of available pores for invasion is higher for a given liquid pressure. Thus, less surface area of the hydrophobic medium is expected to be invaded compared to the hydrophilic medium. Fig. 9 compares the invaded area for the hydrophilic and hydrophobic samples. As encircled in the figure, several areas of the hydrophilic sample are invaded by water forming clusters (Fig. 9(a)). While for the hydrophobic sample (Fig. 9(b)), only two clusters are distinguished.

4.2.2. Progression pattern

The criteria for invading a particular pore are the availability of the pore (proximity to the water frontier) and the capillary pressure required for the pore to be invaded. After the initial invasion, liquid water flows through the thickness of the samples. The pattern for further developments depends on the characteristics of the medium. For a hydrophobic medium, water prefers to move through a path that has already been developed. Thus, excess water injected into the medium after the initial invasion continues to fill the pores which were already invaded. The higher contact angle of the dry pores makes them less vulnerable to future invasion, resulting in no or very few new developments in the water frontier. Fig. 10 compares two consecutive time steps for the hydrophobic sample. To facilitate the comparison between the images, the corresponding time for each image is normalized using the total time of breakthrough ($t^* = t/t_{\text{breakthrough}}$). The first image is chosen as the reference image at $t^* = 0.487$ and the second image shows the new
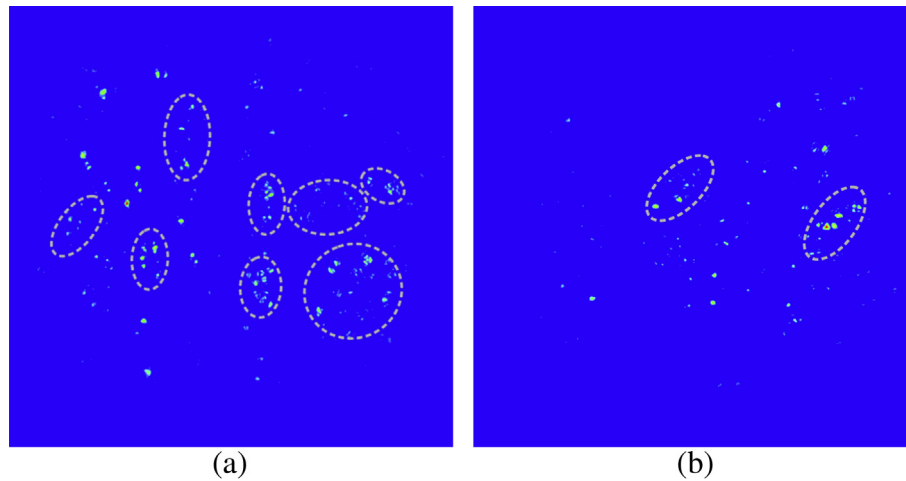
Fig. 9. Initial invasion patterns for (a) hydrophilic (untreated) sample and (b) hydrophobic (treated) sample.

development of invasion pattern in the sample at $t^* = 0.553$. Only three new frontiers are visible in this figure (encircled). For the hydrophilic medium, on the other hand, there is no preferred pattern of invasion. Comparing Fig. 11(a) and (b) (captured at $t^* = 0.487$ and $t^* = 0.554$, respectively) reveals that the new development occurs for the hydrophilic sample and a relatively large area is invaded as flow is developing in the hydrophilic medium compared to the hydrophobic sample.

4.2.3. Pore-filling pattern

For a single empty pore to be invaded by liquid water in a porous medium, a threshold pressure is required. The threshold pressure is determined with respect to the capillary properties of the medium (Eq. (3)). If the medium is hydrophilic the threshold pressure is negative ($\cos\theta < 0$), i.e. the medium intakes the water without resistance and the system reaches to the equilibrium once the medium is saturated. For a hydrophobic medium, the threshold pressure is positive. Thus, the liquid pressure increases, and once it reaches to the threshold pressure it invades the pore. As the saturation of the pore increases the chance for water to invade the adjacent pores increases accordingly. The pressure of the liquid phase also contributes to the invasion process. Thus, one can

quantify the chance of invasion by introducing a hydrodynamic pressure as a pressure correction term, as follows:

$$P_{\text{hydrodynamic}} = S_{\text{pore}} \times P_{\text{ref}} \tag{11}$$

where S_{pore} is the saturation of an individual pore and P_{ref} is the reference pressure which can be replaced by the reservoir pressure for the numerical simulation. For the hydrophobic and hydrophilic samples, the difference between pore saturation and pore-filling processes is illustrated in Fig. 12. The images correspond to $t^* = 0.992$, i.e., an instance right before the breakthrough. For the hydrophobic sample, at least four zones are determined with a high concentration of water (red-color mapping) indicating saturated pores. (For interpretation of the references to color in this figure, the reader is referred to the web version of this article.) For the hydrophilic sample, on the other hand, there is only one highly saturated region though the numbers of invaded pores are higher (as discussed previously). In summary, the main difference between the pore-filling process of hydrophobic and hydrophilic media is that in the hydrophobic sample water continuously fills a single pore until the pore is fully saturated or the phase pressure of water at other locations of the frontier is high enough for another
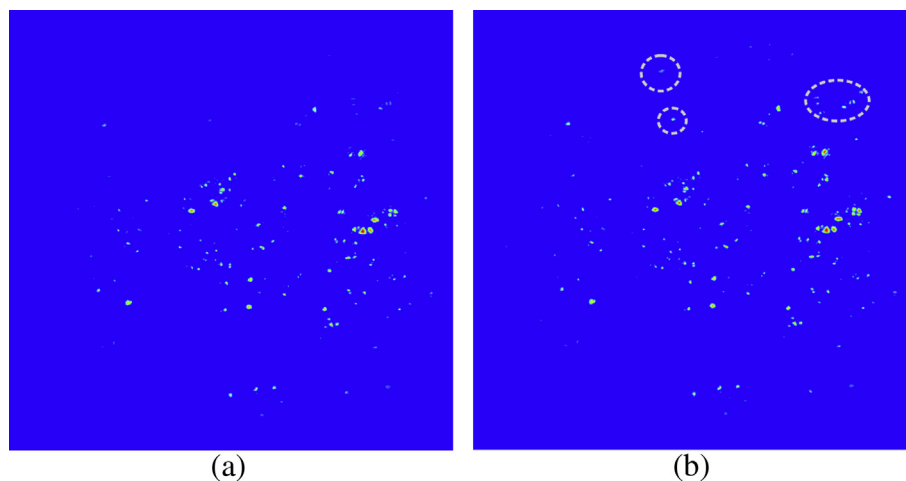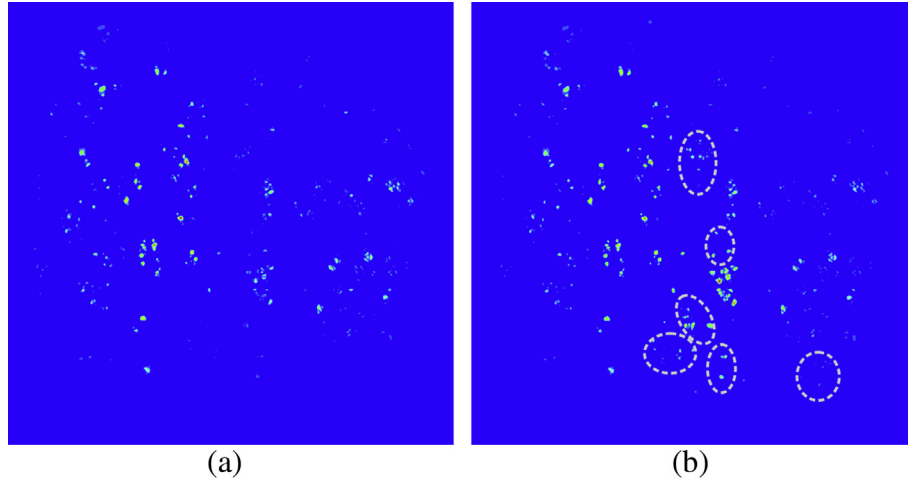

Fig. 10. Progression pattern for treated sample at (a) $t^* = 0.487$ and (b) $t^* = 0.553$.

Fig. 11. Progression pattern for untreated sample at (a) $t^* = 0.487$ and (b) $t^* = 0.554$.

invasion process. In the hydrophilic sample, multiple invasions at different locations of the frontier occur due to a low or negative threshold pressure.

4.3. Modeling

For all the cases studied here, identical network geometry (reference network) is generated (i.e. a network with the same pore size and throat size distributions). Please note that the completely saturated cells ($S_{cell} = 1$) are placed on the catalyst layer ($z^* = 0$), where the color mappings are red. The blue cells represent the pores which are not invaded by water ($S_{cell} = 0$). To verify the validity of the model, the experimental flow characteristic patterns observed for treated and untreated samples are qualitatively compared to those obtained from the model. Then, the algorithm is applied to five hydrophobic fractions ($f = 0.0, 0.1, 0.2, 0.3$ and 0.4) to study the effect of hydrophobicity on the flow configuration. These fractions can be related to the weight percentage of PTFE loading as shown in Ref. [75]. Three replicates of simulation are performed for

each case. Finally, the model is used to determine the total saturation of invading fluid (water), as the hydrophobic fraction increases.

4.3.1. Comparison of numerical results and experimental observations

As explained in Section 4.2, three patterns are observed for the water flow through the GDL. The patterns differ as the hydrophobic fraction of the porous sample increases. In this section, distributions of water saturation obtained from the pore-network modeling for an untreated ($f = 0.0$) and treated samples ($f = 0.40$) are qualitatively compared to the experimental observations for each pattern.

4.3.1.1. Initial invasion pattern. As observed from the experiment, fewer pores are vulnerable to invasion by water in a hydrophobic medium compared to a hydrophilic medium where the number of available pores for invasion is higher. Thus, less surface area of the hydrophobic medium is expected to be invaded compared to the
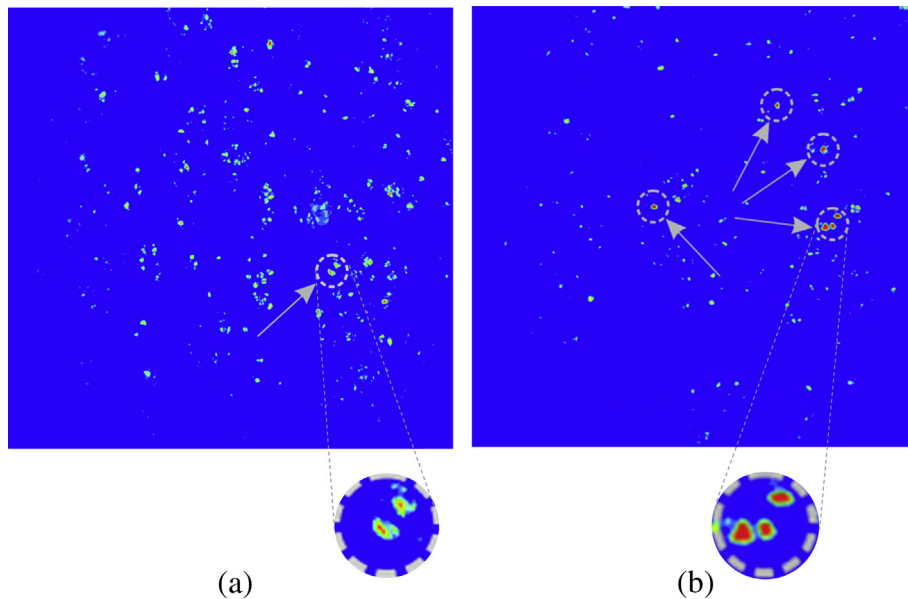

Fig. 12. Pore-filling process for (a) untreated sample and (b) treated sample.

hydrophilic medium. Fig. 13 shows the effect of hydrophobic fraction (f) on the invaded area at the initial stages of invasion ($t^* = 0.25$). The cross-section is chosen to be close to the bottom layer of the sample where the chemical reaction occurs and water is produced ($z^* = 0.25$). For the sample with no hydrophobic agent ($f = 0.0$) all the pores are filled (totally or partially) with water (Fig. 13(a)). As the hydrophobicity increases, the fraction of uninvaded pores increases. For the sample with $f = 0.1$, two uninvaded areas are distinguished (Fig. 13(b)). The same trend is observed as the hydrophobic fraction increases where for the highest

hydrophobic fraction ($f = 0.4$) a comparable area of the sample remains untouched (as encircled in Fig. 13(e)). This is in good agreement with the initial invasion pattern discussed in previous section.

4.3.1.2. Progression pattern. As explained earlier, after the initial invasion liquid water flows through the thickness of the samples and the characteristics of the medium determine the pattern for further developments. For the hydrophobic medium, excess water injected into the medium fills the pores which are already invaded.

(a)

(b)

(c)

(d)

(e)
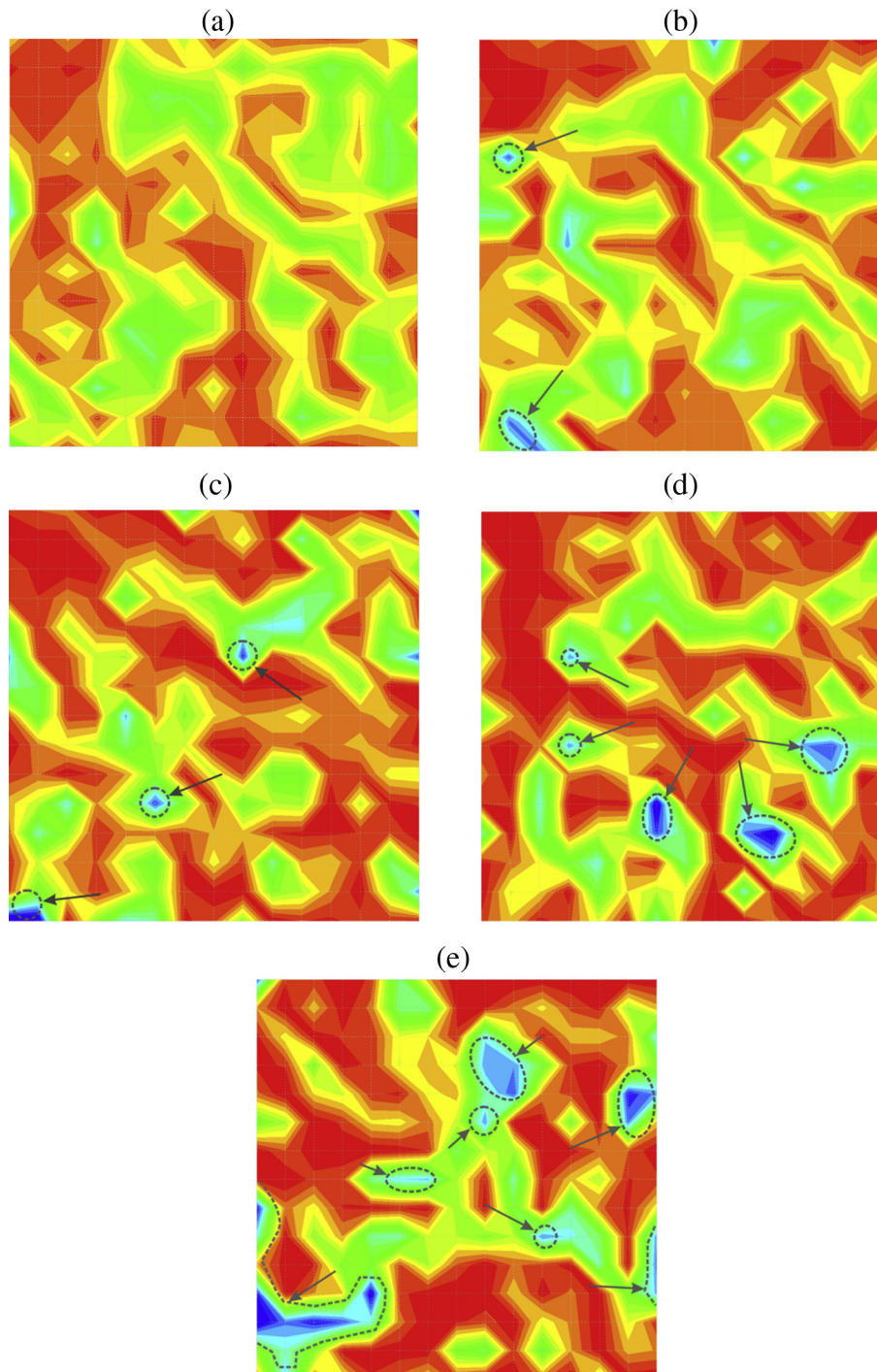
Fig. 13. Numerical results demonstrating the initial invasion pattern at $z^* = 0.25$ for (a) $f = 0.0$, (b) $f = 0.1$, (c) $f = 0.2$, (d) $f = 0.3$, and (e) $f = 0.4$.

In essence, the higher contact angle of the dry pores makes them less vulnerable to future invasion and very little new branching occurs at the water frontier. Fig. 14 shows the numerical results obtained for the hydrophobic sample at $x^* = 0.50$, $y^* = 0.50$ and $z^* = 0.50$ for two consecutive time steps of $t^* = 0.25$ (i.e., reference time) and $t^* = 0.50$. As the figure suggests, only a few new frontiers are visible (encircled) for the hydrophobic medium. For the hydrophilic medium, on the other hand, there is no preferred pattern of invasion and a large area is invaded as flow is developing (Fig. 15(a) and (b)).

4.3.1.3. Pore-filling pattern. As observed experimentally, water continuously fills a single pore in the hydrophobic medium until the pore is fully saturated or the phase pressure of water at other locations of the frontier is high enough for another invasion process. In a hydrophilic medium, on the other hand, multiple invasions at different locations of the frontier occur due to a low or negative threshold pressure, and it is not necessary to have highly saturated pores in order for the invasion process to occur. Fig. 16(a) and (b) shows the numerical results for the untreated and treated samples, respectively. The red-color mapping indicates the highly saturated areas. As the color spectrum gets close to blue, the saturation is reduced. (For interpretation of the references to color in this figure, the reader is referred to the web version of this article.) For the untreated sample (Fig. 16(a)), almost all of the pores in the cross-section ($z^* = 0.25$) are either completely or partially

filled with water. Nevertheless, the number of highly saturated pores is only a few, as shown encircled in the figure. For the treated sample, on the other hand, fewer pores are invaded as indicated by the green-blue areas in Fig. 16(b). In this case, however, water manages to completely fill the invaded pores. Thus, the majority of the invaded pores are highly saturated as indicated in the figure.

4.3.2. Effect of hydrophobicity on the flow pattern

The pore-network model presented is used to study the effect of hydrophobicity on flow pattern and sample saturation. Fig. 17 shows the saturation of each cell at breakthrough. For each hydrophobic fraction, the flow is presented in all three directions. Also, to give a better image of the flow, three slices of the sample are provided in the through-plane directions (at x^*, $y^* = 0.05$, 0.5 and 0.95). For the in-plane direction, a plane close to the top surface of the GDL ($z^* = 0.75$) is presented. The figure suggests that the portion of untouched spots inside the sample is increased as the hydrophobic fraction (f) is increased. In other words, the areas with zero or low saturation (blue-green color mappings) are larger for the samples with higher f. Also, water is uniformly distributed for the sample with no hydrophobic loading ($f = 0.0$) as shown in the first column of the figure, which presents the change in the pattern of water distribution in the planes of $x^* = $ constant. For the same sample, the saturation is constant through the thickness of the GDL, except in the area close to the catalyst layer ($z^* = 0$), where water is produced and obviously local saturation is higher. At the area close
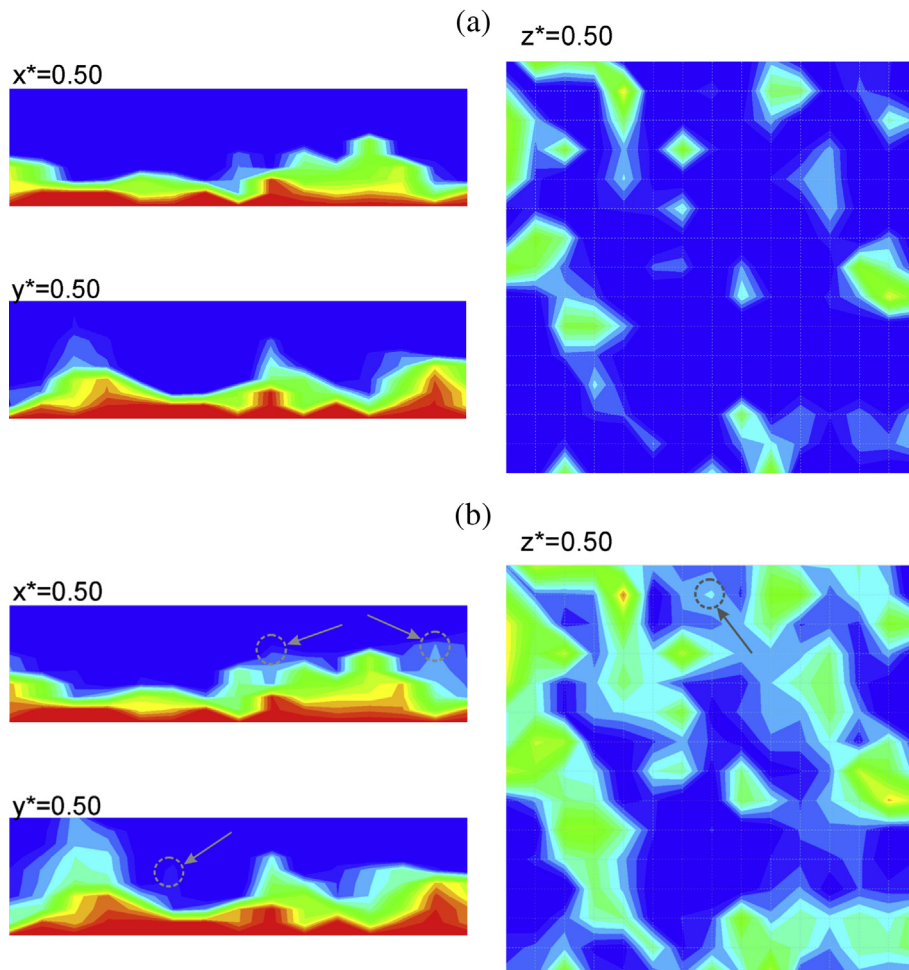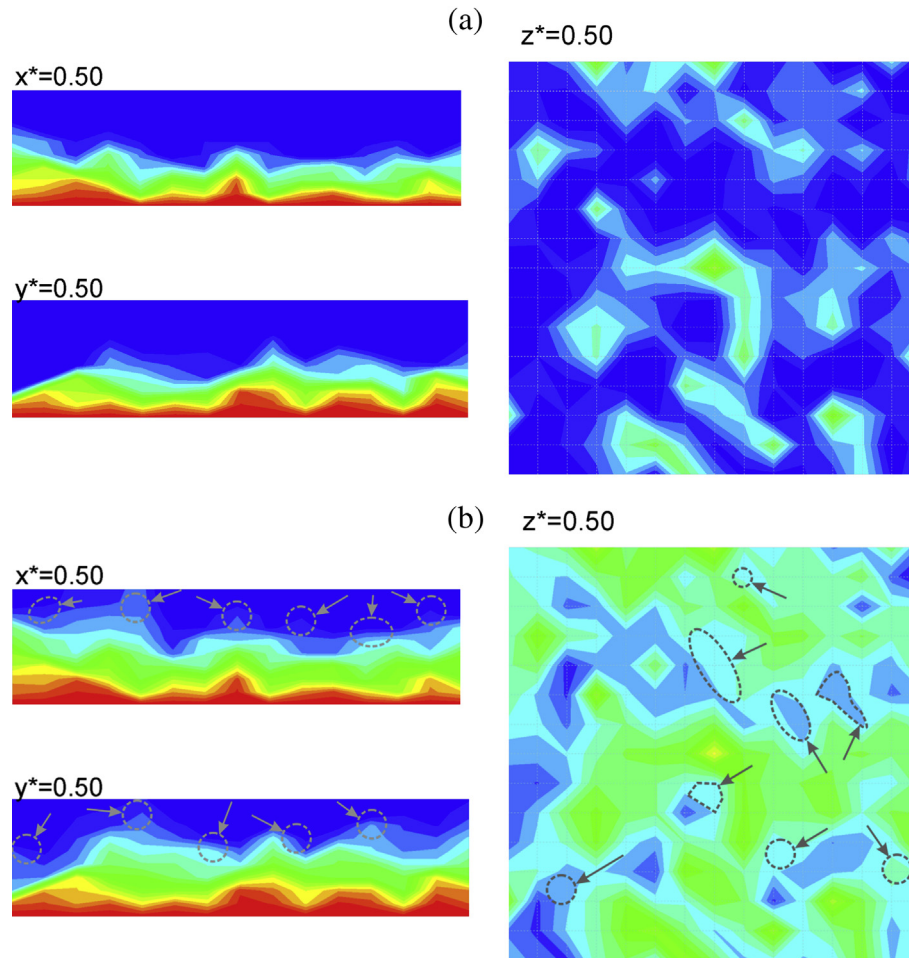

Fig. 14. Numerical results demonstrating the progression pattern for the treated sample ($f = 0.4$) at (a) $t^* = 0.25$, and (b) $t^* = 0.50$.
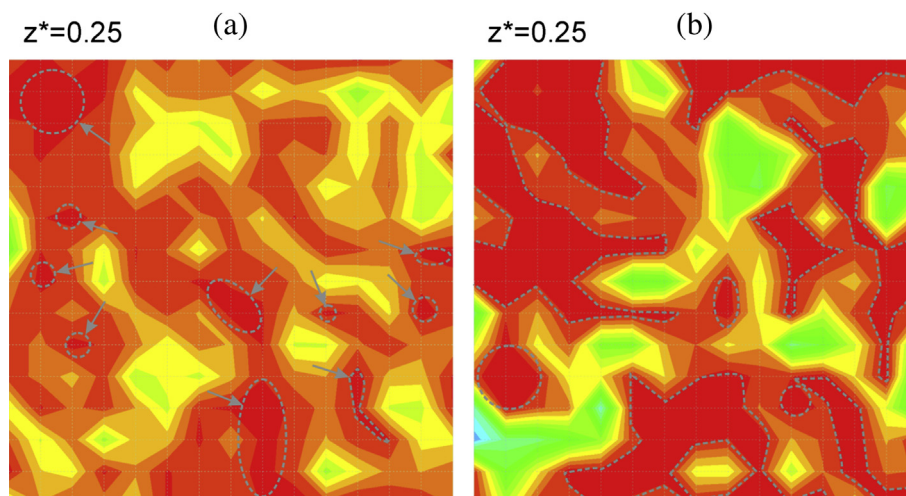
Fig. 15. Numerical results demonstrating the progression pattern for the untreated sample ($f = 0.0$) at (a) $t^* = 0.25$, and (b) $t^* = 0.50$.

to the gas channels ($z^* = 1$), the configuration is not uniform. However, the constant saturation through the thickness of the GDL, especially for the area far from the boundaries ($0 < z^* < 1$), suggests a uniform distribution of water. Also, for the sample with no treatment ($f = 0.0$), there is no preferred path for water to flow through and to find its way out.

As the hydrophobic fraction increases, the pattern of water distribution changes significantly. Although the capillary number (Ca) and mobility ratio ($M = \mu_2/\mu_1$ which is the ratio of viscosity for the displaced and displacing fluids) are almost constant for all the cases studied here, the configuration of water distribution shifts toward viscous-fingering as the hydrophobic fraction increases.

Fig. 16. Numerical results demonstrating the pore-filling pattern for (a) untreated sample ($f = 0.0$), and (b) treated sample ($f = 0.4$).
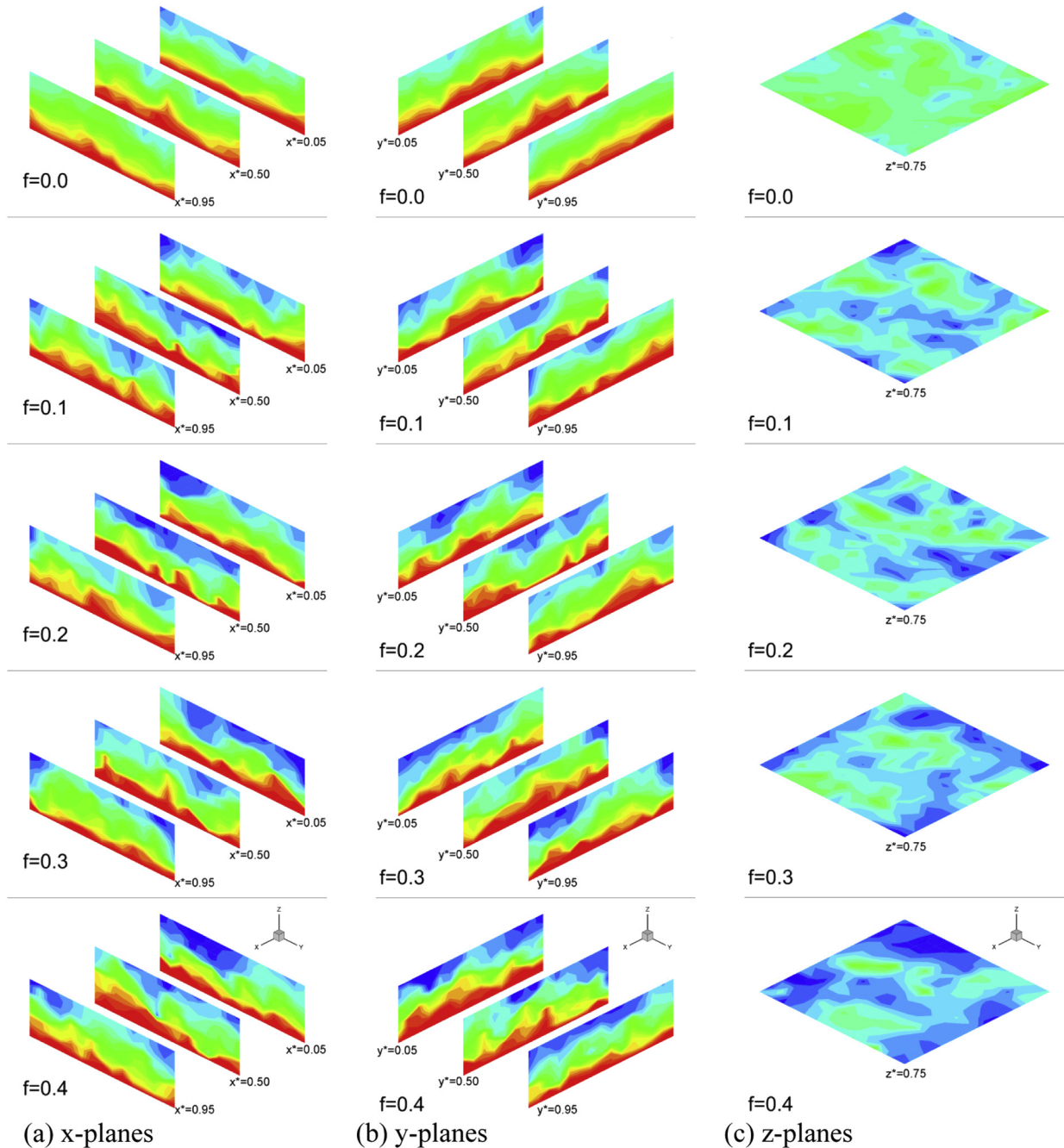
Fig. 17. Effect of hydrophobic fraction on flow configuration at breakthrough ($x^* = x/x_{sample}$, $y^* = y/y_{sample}$ and $z^* = z/z_{sample}$).

Comparison between the flow pattern simulated for the sample with $f = 0.2$ and the sample with no treatment ($f = 0.0$) verifies this fact. For instance, the pattern of water distribution in the mid-plane ($x^* = 0.50$) of the sample with treatment ($f = 0.2$) exhibits four distinguishable peaks in water frontier; while only two peaks are observed for the sample with no treatment ($f = 0.0$). As the hydrophobic fraction further increases, the non-uniformity in the flow pattern develops. As a result of this non-uniformity, a larger surface area close to the gas channel ($z^* = 1$) is untouched by liquid water as shown in the last column of the figure, which presents the distribution of water in a plane parallel to the catalyst layer and close to the gas channel ($z^* = 0.75$). For the sample with no treatment ($f = 0.0$), almost all the surface of this plane is covered with water. The saturation of water is higher compared to the other cases with higher hydrophobic fractions. As the hydrophobic fraction increases, a few blue areas, which indicate the existence of uninvaded cells and pores, on this plane ($z^* = 0.75$) start to develop. These areas provide passages for the reactant gases to pass through and reach to the reaction sites on the catalyst layer.

The model developed here is also used to determine saturation in samples with different hydrophobicity. Fig. 18 shows the saturation curves for difference hydrophobic treatments. For the sample with the highest hydrophobic fraction, the majority of the surface has very low local saturation. The overall saturation is increasing as the hydrophobic content decreases. The pattern presented in this figure is in agreement with those reported in Refs. [73–75].
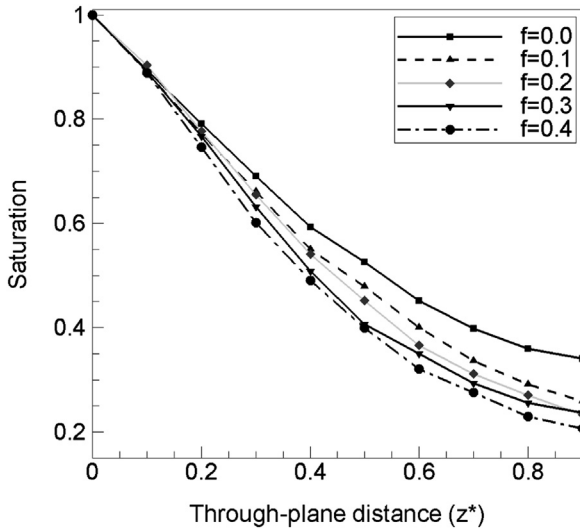
Fig. 18. Effect of the hydrophobic fraction on saturation at the breakthrough.

5. Summary

Image analysis of the fluorescence microscopy technique adopted in this research illustrates the details of phenomena occurring during the flow of liquid water injected into GDL samples. The characteristics of flow are thoroughly studied using the microscopy technique. It is shown that treating the porous sample with the hydrophobic agent drastically changes the initial invasion of water to the medium. For the sample with no treatment (hydrophilic), the majority of the pores on the surface of the sample are available and eventually invaded by the wetting phase. For the treated sample (hydrophobic), a smaller surface of the medium is prone to invasion though the exposed areas of two samples are the same. Liquid water is constantly fed into the porous medium during the injection process. For the treated sample, the feeding channels of liquid water from the surface remain the same during the injection. This is due to the surface properties of the hydrophobic sample which increases the pressure required for any new developments. For the hydrophilic sample, on the other hand, a higher portion of the surface becomes available for invasion as the overall saturation increases during the injection process. Thus, the invasion area expands considerably compared to the hydrophobic sample. The last major difference in the liquid flow pattern between a hydrophobic and hydrophilic sample is the pattern of pore filling. The analysis for this pattern is based on the local saturation of liquid water which is projected into the intensity of the images, i.e. the light intensity is correlated to the pore saturation in each image. Thus, brighter pixels indicate high concentration of liquid water in a particular location. For the hydrophobic samples, the images show small portion of pores withholding water; while for the hydrophilic sample, a relatively large portion of pores contains water. However, the local concentration of water is higher for the hydrophobic sample compared to the hydrophilic one. Using this analysis, the concept of hydrodynamic pressure was developed which was extensively used in the pore-network model. The pore-network model presented in this paper illustrates the details of phenomena underlying the flow of water in GDLs. The microscopic details provided by the model justify the macroscopic properties observed in the experiment. The model confirms higher local saturation (or pore saturation) for hydrophobic medium; while the total medium saturation remains lower compared to the hydrophilic medium (as confirmed by experimental results).

Appendix A. Estimation of water flow rate at the flooding condition

Based on the Faraday's laws

$$m = \left(\frac{Q}{F}\right)\left(\frac{M}{z}\right) \tag{A.1}$$

where m the mass of the substance at the electrode, Q presents the total electric charge passed through the substance, $F = 96{,}485 \ \mathrm{col \ mol^{-1}}$ is the Faraday constant, M is the molar mass of the substance and z is the number of electrons transferred per ion. The derivative of the above equation will yield

$$\frac{\mathrm{d}m}{\mathrm{d}t}\left(\mathrm{gr \ s^{-1}}\right) = \frac{i(A)M(\mathrm{gr \ mol^{-1}})}{zF(\mathrm{col \ mol^{-1}})}$$

$$Q = \frac{\mathrm{d}V}{\mathrm{d}t}\left(\mathrm{m^3 s^{-1}}\right) = \frac{i(A)M(\mathrm{gr \ mol^{-1}})}{zF(\mathrm{col \ mol^{-1}})\rho(\mathrm{gr \ m^{-3}})} \tag{A.2}$$

where i and A present the current and reactive area, respectively. For the reactions occurring in PEM fuel cell, $M = 18.01528 \ \mathrm{gr \ mol^{-1}}$, $\rho = 10^6 \ \mathrm{gr \ m^{-3}}$, and $z = 2$. Thus, the above equation can be rewritten as

$$\frac{\mathrm{d}V}{\mathrm{d}t}\left(\mathrm{m^3 \ s^{-1}}\right) = 9.335 \times 10^{-11}\left(\mathrm{m^3 \ col^{-1}}\right)i(A) \tag{A.3}$$

Substituting the limiting current density of $i = 1.4 \ \mathrm{Acm^{-2}}$ (representing the flooding condition) and the reactive area corresponding to a disk diameter of $d = 3.3$ mm (considered in this paper) in the above equation will result in the water flow rate value of $Q = \mathrm{d}V/\mathrm{d}t = 1.11 \times 10^{-11} \ \mathrm{m^3 s^{-1}}$.

Appendix B. Estimation of hydrophobic pores fraction based on the PTFE loading

The mass of a treated GDL sample (m_{sample}) is the mass of carbon fiber (m_{fiber}) and the PTFE loading (m_{PTFE}):

$$m_{\mathrm{sample}} = m_{\mathrm{fiber}} + m_{\mathrm{PTFE}} \tag{B.1}$$

If the treated sample is represented by a network with *IMAX*, *JMAX* and *KMAX* pores in each direction, using Eq. (B.1) the following correlations hold:

$$\%\mathrm{wt} = \omega = \frac{m_{\mathrm{sample}} - m_{\mathrm{untreated}}}{m_{\mathrm{untreated}}} \times 100$$

$$m_{\mathrm{PTFE}} = \omega m_{\mathrm{fiber}}$$

$$V_{\mathrm{fiber}} = V_{\mathrm{total}} - V_{\mathrm{pore}} = V_{\mathrm{total}}(1 - \varepsilon)$$

$$m_{\mathrm{fiber}} = \rho_{\mathrm{fiber}} V_{\mathrm{total}}(1 - \varepsilon)$$

$$V_{\mathrm{total}} = (IMAX - 1)(JMAX - 1)(KMAX - 1)l_t^3$$

$$m_{\mathrm{fiber}} = \rho_{\mathrm{fiber}}(IMAX - 1)(JMAX - 1)(KMAX - 1)(1 - \varepsilon)l_t^3$$

$$m_{\mathrm{PTFE}} = \omega\rho_{\mathrm{fiber}}(IMAX - 1)(JMAX - 1)(KMAX - 1)(1 - \varepsilon)l_t^3 \tag{B.2}$$

In which m, V and ρ stand for mass, volume and density of each component, respectively, ω is the weight percentage of PTFE loading, ε is the porosity of the sample, and l_t is throat length.

Considering an ultrathin layer of PTFE covers the hydrophobic pore:

$$m_{\text{PTFE}} = N \cdot \rho_{\text{PTFE}} \cdot V_{\text{layer}}$$
$$V_{\text{layer}} = \pi d^2 \delta \tag{B.3}$$

where d and δ present the pore diameter and thickness of the PTFE layer in the pore respectively and N is the total number of hydrophobic pores. The above three equations result in

$$N = \frac{\omega \rho_{\text{fiber}} \left(IMAX - 1 \right) \left(JMAX - 1 \right) \left(KMAX - 1 \right) \left(1 - \varepsilon \right) l_t^3}{\rho_{\text{PTFE}} \cdot \pi d^2 \delta} \tag{B.4}$$

For $\rho_{\text{fiber}} = 400$ kg m^{-3}, $\rho_{\text{PTFE}} = 2200$ kg m^{-3}, $l_t = 11$ μm, $\delta = 0.1$ μm, $\varepsilon = 0.78$, the total number of hydrophobic pores will be

$$N \approx 0.75 \omega (IMAX - 1)(JMAX - 1)(KMAX - 1) \tag{B.5}$$

References

[1] H. Li, Y. Tang, Z. Wang, Z. Shi, S. Wu, D. Song, J. Zhang, K. Fatih, J. Zhang, H. Wang, Z. Liu, R. Abouatallah, A. Mazza, Journal of Power Sources 178 (1) (2008) 103–117.
[2] S. Litster, D. Sinton, N. Djilali, Journal of Power Sources 154 (1) (2006) 95–105.
[3] D. Natarajan, T. Van Nguyen, Journal of Power Sources 115 (1) (2003) 66–80.
[4] F.B. Weng, A. Su, C.Y. Hsu, C.Y. Lee, Journal of Power Sources 157 (2) (2006) 674–680.
[5] T. Berning, N. Djilali, Journal of Power Sources 124 (2) (2003) 440–452.
[6] J. Zawodzinski, A. Thomas, Charles Derouin, Susan Radzinski, J. Ruth Sherman, T. Van Smith, E. Thomas Springer, Shimshon Gottesfeld, Journal of the Electrochemical Society 140 (1993) 1041–1047.
[7] S. Tsushima, K. Teranishi, S. Hirai, Electrochemical and Solid-state Letters 7 (2004) A269.
[8] S. Tsushima, K. Teranishi, S. Hirai, Energy 30 (2) (2005) 235–245.
[9] K. Teranishi, S. Tsushima, S. Hirai, Electrochemical and Solid-state Letters 8 (2005) A281.
[10] K. Feindel, L. LaRocque, D. Starke, S. Bergens, R. Wasylishen, Journal of the American Chemical Society 126 (37) (2004) 11436–11437.
[11] K. Feindel, S. Bergens, R. Wasylishen, Journal of the American Chemical Society 128 (43) (2006) 14192–14199.
[12] A. Bazylak, International Journal of Hydrogen Energy 34 (9) (2009) 3845–3857.
[13] R. Mosdale, G. Gebel, M. Pineri, Journal of Membrane Science 118 (2) (1996) 269–277.
[14] R. Satija, D. Jacobson, M. Arif, S. Werner, Journal of Power Sources 129 (2) (2004) 238–245.
[15] N. Pekula, K. Heller, P. Chuang, A. Turhan, M. Mench, J. Brenizer, K. Ünlü, Nuclear Instruments and Methods in Physics Research Section A: Accelerators, Spectrometers, Detectors and Associated Equipment 542 (1) (2005) 134–141.
[16] T. Trabold, J. Owejan, D. Jacobson, M. Arif, P. Huffman, International Journal of Heat and Mass Transfer 49 (25) (2006) 4712–4720.
[17] J. Owejan, T. Trabold, D. Jacobson, D. Baker, D. Hussey, M. Arif, International Journal of Heat and Mass Transfer 49 (25) (2006) 4721–4731.
[18] A. Turhan, K. Heller, J. Brenizer, M. Mench, Journal of Power Sources 160 (2) (2006) 1195–1203.
[19] J. Zhang, D. Kramer, R. Shimoi, Y. Ono, E. Lehmann, A. Wokaun, K. Shinohara, G. Scherer, Electrochimica Acta 51 (13) (2006) 2715–2727.
[20] J. Siegel, D. McKay, A. Stefanopoulou, D. Hussey, D. Jacobson, Journal of the Electrochemical Society 155 (2008) B1168.
[21] R. Bellows, M. Lin, M. Arif, A. Thompson, D. Jacobson, Journal of the Electrochemical Society 146 (1999) 1099.
[22] T.A. Zawodzinski Jr., T.E. Springer, F. Uribe, S. Gottesfeld, Solid State Ionics 60 (1–3) (1993) 199–211.
[23] T.E. Springer, T.A. Zawodzinski, S. Gottesfeld, Journal of the Electrochemical Society 138 (8) (1991) 2334–2342.
[24] M. Hickner, N. Siegel, K. Chen, D. McBrayer, D. Hussey, D. Jacobson, M. Arif, Journal of the Electrochemical Society 153 (2006) A902.
[25] J. Owejan, T. Trabold, D. Jacobson, M. Arif, S. Kandlikar, International Journal of Hydrogen Energy 32 (17) (2007) 4489–4502.
[26] S. Kim, M. Mench, Journal of the Electrochemical Society 156 (2009) B353.
[27] P. Sinha, P. Halleck, C. Wang, Electrochemical and Solid-state Letters 9 (2006) A344.
[28] I. Manke, C. Hartnig, M. Grunerbel, W. Lehnert, N. Kardjilov, A. Haibel, A. Hilger, J. Banhart, H. Riesemeier, Applied Physics Letters 90 (17) (2007) 174105.
[29] U. Pasaogullari, C. Wang, Journal of the Electrochemical Society 152 (2005) A380.
[30] S. Lee, N. Lim, S. Kim, G. Park, C. Kim, Journal of Power Sources 185 (2) (2008) 867–870.
[31] C. Hartnig, I. Manke, R. Kuhn, N. Kardjilov, J. Banhart, W. Lehnert, Applied Physics Letters 92 (13) (2008) 134106.
[32] K. Tüber, D. Pócza, C. Hebling, Journal of Power Sources 124 (2) (2003) 403–414.
[33] A. Hakenjos, H. Muenter, U. Wittstadt, C. Hebling, Journal of Power Sources 131 (1) (2004) 213–216.
[34] X. Yang, F. Zhang, A. Lubawy, C. Wang, Electrochemical and Solid-state Letters 7 (2004) A408.
[35] J. Borrelli, S. Kandlikar, T. Trabold, and J. Owejan. Water transport visualization and two-phase pressure drop measurements in a simulated pemfc cathode minichannel, in: Proceedings of third international conference on microchannels and minichannels, Toronto, Canada, 2005.
[36] K. Sugiura, M. Nakata, T. Yodo, Y. Nishiguchi, M. Yamauchi, Y. Itoh, Journal of Power Sources 145 (2) (2005) 526–533.
[37] S. Ge, C. Wang, Journal of the Electrochemical Society 154 (2007) B998.
[38] E. Kumbur, K. Sharp, M. Mench, Journal of Power Sources 161 (1) (2006) 333–345.
[39] D. Spernjak, A. Prasad, S. Advani, Journal of Power Sources 170 (2) (2007) 334–344.
[40] A. Theodorakakos, T. Ous, M. Gavaises, J. Nouri, N. Nikolopoulos, H. Yanagihara, Journal of Colloid and Interface Science 300 (2) (2006) 673–687.
[41] F. Weng, A. Su, C. Hsu, C. Lee, Journal of Power Sources 157 (2) (2006) 674–680.
[42] E. Kimball, T. Whitaker, Y. Kevrekidis, J. Benziger, AIChE Journal 54 (5) (2008) 1313–1332.
[43] J.H. Nam, M. Kaviany, International Journal of Heat and Mass Transfer 46 (24) (2003) 4595–4611.
[44] U. Pasaogullari, C.Y. Wang, Journal of the Electrochemical Society 151 (3) (2004) A399–A406.
[45] A. Bazylak, D. Sinton, Z. Liu, N. Djilali, Journal of Power Sources 163 (2) (2007) 784–792.
[46] A. Bazylak, D. Sinton, N. Djilali, Journal of Power Sources 176 (1) (2008) 240–246.
[47] A. Bazylak, J. Heinrich, N. Djilali, D. Sinton, Journal of Power Sources 185 (2) (2008) 1147–1153.
[48] A.K. Singhal, W.H. Somerton, Oil and Gas Science and Technology 32 (6) (1977) 897–920.
[49] K.K. Mohanty, H.T. Davis and L.E. Scriven. Paper SPE 9406. SPE Annual Technical Conference and Exhibition, 1980.
[50] A.C. Payatakes, K.M. Ng, R.W. Flumerfelt, AIChE Journal 26 (3) (1980) 430–443.
[51] J. Koplik, T.J. Lasseter, Chemical Engineering Communications 26 (4) (1984) 285–295.
[52] J. Koplik, T.J. Lasseter, Old SPE Journal 25 (1) (1985) 89–100.
[53] M.M. Dias, A.C. Payatakes, Journal of Fluid Mechanics Digital Archive 164 (2006) 305–336.
[54] D.F. Leclerc, G.H. Neale, Journal of Physics A: Mathmatics and General 21 (1988) 2979–2994.
[55] R. Lenormand, C. Zacone, SPE Formation Evaluation 3 (1) (1988) 271–275.
[56] J.T. Gostick, M.A. Ioannidis, M.W. Fowler, M.D. Pritzker, Journal of Power Sources 173 (1) (2007) 277–290.
[57] P.K. Sinha, C.Y. Wang, Electrochimica Acta 52 (28) (2007) 7936–7945.
[58] P.K. Sinha, C.Y. Wang, Chemical Engineering Science 63 (4) (2008) 1081–1091.
[59] O. Chapuis, M. Prat, M. Quintard, E. Chane-Kane, O. Guillot, N. Mayer, Journal of Power Sources 178 (1) (2008) 258–268.
[60] B. Markicevic, N. Djilali, Journal of Power Sources 196 (5) (2011) 2725–2734.
[61] M. Blunt, SPE Journal 2 (1) (1997) 70–87.
[62] S.P. Kuttanikkad, M. Prat, J. Pauchet, Journal of Power Sources 196 (3) (2011) 1145–1155.
[63] J.D. Fairweather, P. Cheung, D.T. Schwartz, Journal of Power Sources 195 (3) (2010) 787–793.
[64] M. El Hannach, J. Paucheta, M. Prat, Electrochimica Acta 56 (2011) 10796–10808.
[65] M. Blunt, Journal of Petroleum Science and Engineering 20 (3) (1998) 117–125.
[66] J. Pauchet, M. Prat, P. Schott, S.P. Kuttanikkad, International Journal of Hydrogen Energy 37 (2012) 1628–1641.
[67] J.H. Kang, K.N. Kim, J.H. Nam, C.J. Kim, International Journal of Hydrogen Energy 37 (2012) 1642–1652.
[68] K.J. Lee, J.H. Nam, C.J. Kim, Journal of Power Sources 195 (1) (2010) 130–141.
[69] R. Wu, Q. Liao, X. Zhu, H. Wang, International Journal of Heat and Mass Transfer 55 (2012) 2581–2589.
[70] R. Wu, Q. Liao, X. Zhu, H. Wang, International Journal of Hydrogen Energy 37 (2012) 1255–11267.
[71] J.R. Lakowicz, Principles of Fluorescence Spectroscopy, second ed., Kluwer Academic/Plenum Publishers, 1999.
[72] M. Mathias, J. Roth, J. Fleming, W. Lehnert, Diffusion media materials and characterization, in: Handbook of Fuel Cells – Fundamentals, Technology and Applications, vol.3, Wiley Online Library, 2003, pp. 517–537.
[73] U. Pasaogullari, C.Y. Wang, Electrochimica Acta 49 (25) (2004) 4359–4369.
[74] S. Park, J.W. Lee, B.N. Popov, Journal of Power Sources 177 (2) (2008) 457–463.
[75] S. Park, B.N. Popov, Electrochimica Acta 54 (12) (2009) 3473–3479.
[76] S. Park, B.N. Popov, Fuel 90 (1) (2011) 436–440.
[77] S. Park, J.W. Lee, B.N. Popov, International Journal of Hydrogen Energy 37 (7) (2012) 5850–5865.
[78] N. Zamel, X. Li, J. Becker, A. Wiegmann, International Journal of Hydrogen Energy 36 (9) (2011) 5466–5478.
[79] A.Z. Weber, R.M. Darling, J. Newman, Journal of Electrochemical Society 151 (10) (2004) A1715–A1727.